INSTRUMENTS AND METHODS OF INVESTIGATION

Accelerator-based neutron source for boron neutron capture therapy

A A Ivanov, A N Smirnov, S Yu Taskaev, B F Bayanov, Yu I Belchenko,
V I Davydenko, A Dunaevsky, I S Emelev, D A Kasatov, A N Makarov,
M Meekins, N K Kuksanov, S S Popov, R A Salimov, A L Sanin, I N Sorokin,
T V Sycheva, I M Shudlo, D S Vorob'ev, V G Cherepkov, S N Fadeev

Contents

Abstract. An accelerator-based neutron source is being developed for boron neutron capture therapy (BNCT) of oncological diseases. In the source, neutrons are produced through interaction of a proton beam accelerated in an electrostatic tandem accelerator with a lithium target. The source generates an optimal neutron beam for BNCT treatment, and has several unique practical characteristics that make it ideally suited for clinical use. Namely, the tandem accelerator is compact (its design does not utilize accelerator tubes), reliable, simple and flexible in operation, and relatively inexpensive. The paper provides a comprehensive overview of studies of the neutron source prototype and preliminary test results of the first specialized neutron source for clinical trials of BNCT.

Keywords: accelerator-based neutron source, electrostatic accelerator, boron neutron capture therapy, negative hydrogen ion source

A A Ivanov [(1, a)], **A N Smirnov** [(2, 3, b)], **S Yu Taskaev** [(1, 4, c)],
B F Bayanov [(1, d)], **Yu I Belchenko** [(1, e)], **V I Davydenko** [(1, f)],
A Dunaevsky [(3)], **I S Emelev** [(1, 4, g)], **D A Kasatov** [(1, 4, h)],
A N Makarov [(1, 4, i)], **M Meekins** [(3)], **N K Kuksanov** [(1, j)],
S S Popov [(1, k)], **R A Salimov** [(1)], **A L Sanin** [(1, l)],
I N Sorokin [(1, 3, m)], **T V Sycheva** [(1, 4)], **I M Shudlo** [(1, 4, n)],
D S Vorob'ev [(1, o)], **V G Cherepkov** [(1, p)], **S N Fadeev** [(1, q)]

(1) Budker Institute of Nuclear Physics,
    Siberian Branch of the Russian Academy of Sciences,
    prosp. Akademika Lavrent'eva 11, 630090 Novosibirsk,
    Russian Federation
(2) TAE Life Sciences, 19631 Pauling, Foothill Ranch, CA, 92610, USA
(3) TAE Technologies, 19631 Pauling, Foothill Ranch, CA, 92610, USA
(4) Novosibirsk State University, ul. Pirogova 2, 630090 Novosibirsk,
    Russian Federation
E-mail: (a)aaivanov5353@mail.ru, (b)ASmirnov@tae.com,
   (c)S.Yu.Taskaev@inp.nsk.su, (d)B.F.Bayanov@inp.nsk.su,
   (e)Yu.I.Belchenko@inp.nsk.su, (f) V.I.Davydenko@inp.nsk.su,
   (g) I.S.Emelev@inp.nsk.su, (h)D.A.Kasatov@inp.nsk.su,
   (i)A.N.Makarov@inp.nsk.su, (j) N.K.Kuksanov@inp.nsk.su,
   (k) S.S.Popov@inp.nsk.su, (l) A.L.Sanin@inp.nsk.su,
   (m) I.N.Sorokin@inp.nsk.su, (n)cshudlo.i.m@gmail.com,
   (o) D.S.Vorobev@inp.nsk.su, (p) V.G.Cherepkov@inp.nsk.su,
   (q) S.N.Fadeev@inp.nsk.su

1. Introduction

Boron neutron capture therapy (BNCT) is one of the promising methods for the treatment of malignant tumors [1–3]. With this therapy, the patient is given a drug containing a harmless stable isotope ^{10}B that selectively accumulates in cancer cells. Then, the peritumoral area in the patient's body is irradiated with neutrons that enter into a reaction with boron nuclei. The cross section of the capture of thermal neutrons by the ^{10}B nucleus is anomalously large[1] — 3387 b. Absorption of a neutron by the ^{10}B nucleus leads to an instantaneous nuclear reaction $^{10}B(n, \alpha)^7Li$, releasing 2.79 MeV of energy. In 6.1% of the cases, the energy is distributed only between the lithium nucleus and the α-particle; in the remaining 93.9% of the cases, the lithium

---

[1] There are other nuclei, e.g., ^{113}Cd, ^{135}Xe, ^{149}Sm, ^{151}Eu, ^{155}Gd, ^{157}Gd, ^{147}Hf, ^{199}Hg with a large absorption cross section of the thermal neutron. However, in most of them, the neutron capture is accompanied by neutron and γ-radiation, which does not ensure the locality of energy release in soft tissues.

nucleus flies out in an excited state and emits a γ-quantum with an energy of 0.48 MeV. The products of the nuclear reaction (a lithium nucleus with an energy of 0.84 MeV and an α-particle with an energy of 1.47 MeV) have a short range in water or in body tissues: 5.2 and 7.5 μm, respectively (the typical size of mammalian cells). The deceleration rate of the γ-quantum is significantly lower (0.3 keV μm^{-1}). Thus, the release of the main part of the energy of the nuclear reaction $^{10}B(n, \alpha)^{7}Li$ (84%) is limited by the size of a single cell, and the selective accumulation of boron inside tumor cells and subsequent irradiation with neutrons should lead to their destruction with relatively little damage to the surrounding normal cells.

In comparison to traditional radiation therapy using X-rays and proton beams, BNCT has a number of unique advantages. The targeted delivery of boron to cancer cells by biochemical methods provides enhanced selectivity of the cellular effect compared to that in traditional radiotherapy, where it depends on the accuracy of physical focusing of the beams in the tumor. The relative biological efficiency of BNCT is approximately three times that of traditional methods, since cells are destroyed by heavier particles, such as Li and He nuclei. The increased selectivity of BNCT makes possible its application for poorly localized diffuse tumors refractory to conventional therapies. In addition, BNCT can be performed in one session, while the currently widely used fractional X-ray or proton radiotherapy requires accumulation of a therapeutic dose of radiation over many sessions during several weeks. The severity of side effects and the overall level of toxicity associated with BNCT are significantly lowered, improving the quality of life and the well-being of patients during treatment, as has been confirmed in many clinical trials of BNCT.

Moreover, the throughput of a BNCT clinic increases many times, which makes it possible to offer this type of therapy to a much larger number of patients.

The foundations of the BNCT technique were laid in experiments with reactor neutron sources [4–23]. Early studies [6, 7] failed to demonstrate a high therapeutic efficacy of the method. They used imperfect preparations for boron delivery which did not allow high concentrations of boron and the necessary selectivity of its action in cancer cells to be achieved. In the course of time, significant progress was made due to the use of improved low-molecular weight drugs, such as sodium boroncaptate $Na_2B_{12}H_{11}SH$ (BSH) [8, 9] and boronphenylalanine $(HO)_2{}^{10}B-C_6H_4-CH_2CH(NH_2)-CO_2H$ (BPA) [10]. BSH and BPA preparations produce a boron concentration of 15–20 ppm (parts per million) in normal tissues and 60–70 ppm in tumors. As a result, there is about three to four times the difference between boron concentrations (contrast ratio) in the tumor cells and the surrounding normal tissues. The use of these drugs provides a basis for very successful clinical trials. The impressive initial results reported in Refs [9, 10] made it possible to move on to clinical studies of BNCT for the treatment of deep-seated intracerebral tumors.

Subsequently, the area of application of the BNCT technique was successfully extended to many other types of tumors [19–23]. However, the development of BNCT from a promising research technique to a commercially available medical technology has until recently been limited by two closely related factors. First of all, it should be noted that the inaccessibility of nuclear reactors and the inconvenience of their use as neutron sources prevented access to BNCT for

oncologists and patients. This significantly restricted the extent and the frequency of clinical trials. The lack of promising large-scale clinical studies, in turn, limited interest in BNCT in the pharmacological community and did not promote the development of more advanced drugs for targeted boron delivery.

The efficiency of BNCT is determined by the parameters of the neutron beam, the concentration of boron in cancerous and normal cells, and the contrast ratio. The quality of treatment is characterized by two parameters: the therapeutic ratio and the depth of therapy. The therapeutic ratio is the ratio of the maximum dose rate in the tumor to that in normal tissues. The depth of therapy is the distance from the skin and the underlying layer down to which the dose rate in the tumor exceeds the maximum dose rate in normal tissues. Investigations have demonstrated that, when BPA and BSH are applied, the therapeutic beam must provide a flux density of epithermal neutrons (0.5 eV–10 keV) on the surface of the patient's body above 10^9 cm^{-2} s^{-1}, so that the duration of irradiation is less than 1 hour. The use of epithermal neutrons is dictated by the necessity to obtain the maximum density of thermal neutrons at the depth of the tumor's location. Fluxes of slow neutrons, fast neutrons, and γ-radiation may be present in a therapeutic beam. The use of slow neutrons requires an additional nonlocalized dose due to their absorption by nitrogen or hydrogen, with the emission of a proton and a γ-quantum, respectively. The use of fast neutrons is associated, as a result of elastic scattering mainly on hydrogen nuclei, with the appearance of recoil protons and makes a significant contribution to the dose on the surface. Neutron beams of nuclear reactors ensure a dose rate of 0.2–2 Sv min^{-1}, a therapeutic ratio of 4–6, and a therapy depth of 8 to 10 cm [3].

At present, studies in the field of BNCT have gained a new impetus due to the appearance of accelerator-based neutron sources [24–37] that permit obtaining the desired parameters of neutron fluxes. Moreover, such sources are characterized by enhanced safety, small size, and relatively low cost, which makes it possible to place them directly in a clinical setting. This creates ideal conditions for conducting extensive clinical trials and studies of new drugs for the targeted boron delivery. An important practical achievement was the commercial licensing of BNCT using an accelerator-driven neutron source in combination with a BPA drug for the treatment of malignant brain tumors in Japan [38]. This should speed up the licensing of this treatment modality in other countries.

It is expected that a similar license will soon be obtained for the treatment of head and neck tumors [39]. In Europe, China, Russia, the USA, and Japan, active work is underway to create more advanced carriers for boron delivery [40]. A number of new promising drugs have been proposed, including boron-containing porphyrins [41], nucleosides [42], peptides [43], monoclonal antibodies [44], liposomes [45], nanoparticles of various types [46], co-polymers [47], and polyhedral boranes [48]. *In vitro* laboratory studies have demonstrated that the selectivity (contrast ratio) of some new compounds is 10–100 times that of BPA and BSH, which will undoubtedly lead to tremendous progress in the clinical use of BNCT in the near future.

To generate neutrons in accelerator-based sources, nuclear reactions are used that occur when various targets are bombarded by accelerated beams of charged particles [3, 24, 25]. Especially attractive are the endothermal reactions

^{7}Li(p, n)^{7}Be, ^{9}Be(p, n)^{9}B, and ^{12}C(d, n)^{13}N that do not require too high a beam energy, which allows the use of very compact accelerators that can be conveniently placed in a clinical setting. The most promising reaction is an endothermic one, ^{7}Li(p, n)^{7}Be, with a threshold of 1.88 MeV, which has a sufficiently large cross section above the threshold and makes it possible to obtain low-energy neutrons in the near-threshold regime. To obtain accelerated beams in a desired range of currents and energies, various types of cyclic (cyclotrons) [26, 27] and linear (electrostatic and radio frequency) accelerators are used [28–37]. A review of currently available accelerator-based neutron sources for BNCT can be found in Ref. [25].

A neutron source based on an electrostatic tandem accelerator has been created at the Budker Institute of Nuclear Physics, Siberian Branch of the Russian Academy of Sciences (BINP), Novosibirsk jointly with TAE Life Sciences (USA). This facility is ideal for BNCT under clinical conditions. The neutron source developed specially for BNCT has a number of advantages over other sources. It uses a lithium target to generate neutrons, and its beam, unlike that in cyclotrons, has a relatively low energy (~ 2.5 MeV), which accounts for its optimal characteristics. Cyclotrons have lower currents than linear accelerators, at a much higher energy. Most often, neutron sources for BNCT using cyclotrons operate with a beryllium target, and the fast component predominates in the neutron spectrum. The presence of a fast component has an extremely negative effect on the results of BNCT. To slow down neutrons and suppress the fast component, a bulky and expensive neutron beam shaping assembly (BSA) is used that is unable to produce the optimal neutron energy spectrum for BNCT. Compared to other electrostatic accelerators, the tandem accelerator is compact, has a relatively simple design of the power supply system, and shows high reliability (note that the maximum electric potential in the tandem system is only half of the total energy of the proton beam). Owing to the use of electrostatic technology, the tandem accelerator is simple and flexible in operation as well as relatively cheap, which favorably distinguishes it, say, from high-frequency linear accelerators. Sections 2–5 discuss the features of the neutron source and the main results of research conducted over a number of years, first on the prototype of the neutron source, then on a version of it intended for clinical trials.

2. Neutron source based on a BINP tandem accelerator

In 1998, researchers from the BINP SB RAS (Novosibirsk) and the Institute of Physics and Power Engineering (Obninsk) proposed an accelerator-based neutron source for fast-neutron therapy and neutron capture therapy [36]. To generate a high-current proton beam, this source uses a tandem accelerator with an original electrode design, without traditional accelerating tubes. The main idea was to move the inter-electrode insulators away from the charged particle beam and thereby to improve the high voltage strength. Neutrons are generated by a lithium target irradiated with an accelerated proton beam. Initially, it was proposed that a near-threshold neutron generation regime in which the generated particles fly predominantly forward and have a relatively low energy (about 40 keV) due to kinematic collimation be used for therapy.

A schematic of the proposed tandem accelerator is presented in Fig. 1. A beam of negative hydrogen ions is introduced into the tandem accelerator; thereafter, it is accelerated by positive potential U applied to the central electrode of the tandem. After stripping in a gas target mounted on the central electrode, the proton beam is accelerated by the same potential to an energy of $2eU$. The key advantages in this case are the installation of an ion source at ground potential and a reduction in the necessary accelerating voltage by half, which simplify electrostatic isolation and, therefore, reduce the size and the cost of the accelerator.

Configuration of the accelerator markedly differs from the standard one due to the absence of accelerating tubes. The internal electrodes of the accelerator are fixed on a single bushing insulator (see Fig. 1). The potential of the high-voltage electrode of the gas-filled high-voltage source is transferred to the tandem electrode through a pipe that tightens both parts of the bushing insulator. The potential distribution over the electrodes of the gas-filled bushing insulator is set by the resistive divider. The respective potentials are transferred to electrodes placed in a vacuum in the upper part of the accelerator using a system of internal coaxial cylinders connecting the electrodes of the lower (gas) and the upper (vacuum) parts of the bushing insulator. The vacuum part of the bushing is assembled from annular glass
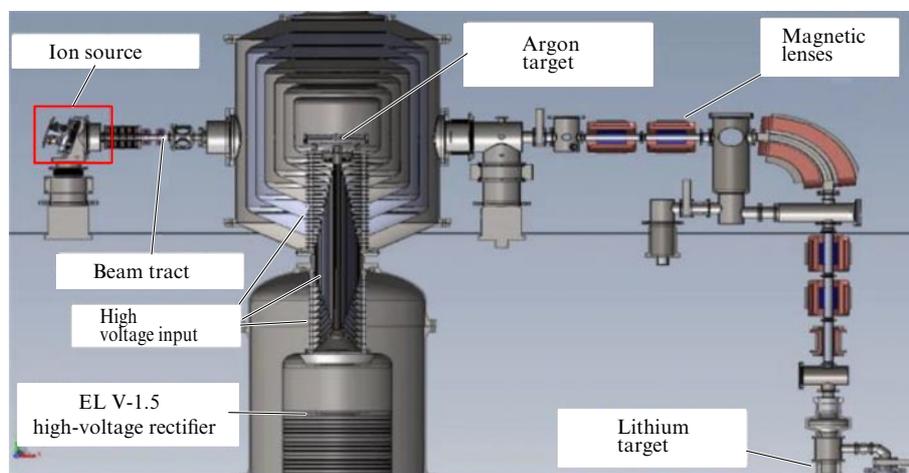
Figure 1. (Color online.) Schematic of the BINP tandem accelerator.

insulators with accelerator electrodes inserted between them. Initially, indium was used for vacuum sealing of the bushing, which required a long time for the seals to shrink. In addition, indium seals proved unreliable, which resulted in leakage. Subsequently, the indium seals were replaced by rubber seals with simultaneous improvement in the sealing flanges.

Intermediate cylindrical tandem electrodes located coaxially with the high-voltage electrode and the vacuum tank are fixed on the electrodes in the upper part of the bushing insulator. The electrode potentials determine the potential distribution along the accelerating path. The electric field strength in the inter-electrode gap at a voltage of 1 MV is ~ 25 kV cm^{-1}. The total area of the tandem electrodes is several ten square meters.

The low-energy beam of negative hydrogen ions is formed by the ion source and is focused by the magnetic solenoid lens onto the input of the accelerator, where it is accelerated to an energy of 1–1.15 MeV. In the stripping target installed inside the central electrode, negative hydrogen ions are converted into protons, which are then accelerated to 2–2.3 MeV. The gas is pumped out of the target by a set of turbomolecular and cryogenic pumps through holes in the electrodes and the beam path. To prevent breakdowns, the holes in the electrodes are closed with special shutters. A variant of the target with argon recirculation was also considered [49]. To ensure recirculation, an additional recirculation chamber with small apertures is installed inside the high-voltage electrode for beam passage. The argon leaving the stripping target is intensively pumped out by a turbomolecular pump installed inside the chamber, the outlet of which is connected to the stripping target. Estimates show that recirculation makes it possible to reduce the argon flow into the accelerator gaps to less than one tenth. The target without recirculation is used in the accelerator.

The accelerated beam enters the high-energy beam transport duct. It ensures the transmission of the proton beam with an energy of ~ 2 MeV that has emerged from the accelerator to the neutron-generating target. In the path, the beam is focused by a pair of quadrupole lenses and is deflected by 90° in the vertical plane by a bending magnet. In the vertical part of the high-energy duct, the beam is again focused by the pair of quadrupole lenses, passes through the magnetic scanning system, and hits the target.

During the commissioning of the tandem accelerator, its design was improved, and the algorithm of high-voltage training with an automatic voltage increase was developed. The algorithm envisaged the measurement of dark currents of the accelerator and the stepwise rise in voltage to a predetermined level when they dropped [50].

A procedure for separate training of individual tandem clearances after assembly was also applied. The reliability of the accelerator was enhanced by implementing a set of measures, such as improving vacuum seals and the material and shape of ring insulators in the bushing, together with optimizing the shape of the electrodes to reduce the electric field strength on their surfaces. Figure 2 shows the dynamics of voltage growth at the high-voltage electrode of the tandem accelerator due to the improvement in bushing design since commissioning in 2005.

2.1 Surface-plasma source of negative ions

Injections into the BINP tandem accelerator are made using a surface-plasma source of negative ions. Initially, it was proposed in [37] that a stationary source of negative ions
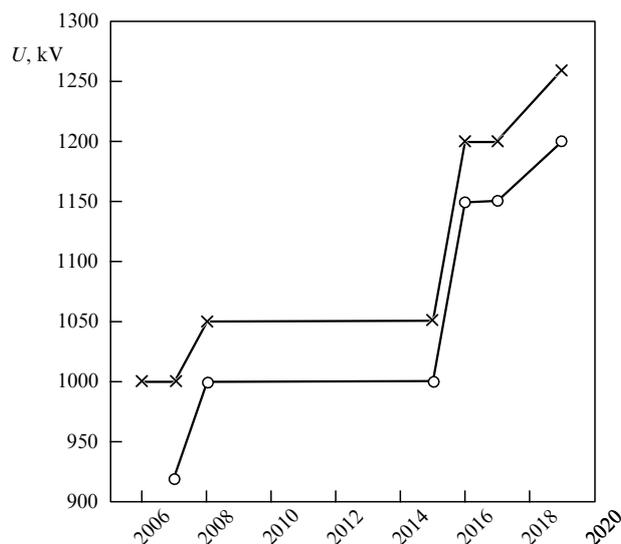
Figure 2. Voltage dynamics during the development and improvement of the tandem: X's indicate maximum voltage values with breakdowns, circles are voltage without breakdowns for more than 1 hour.
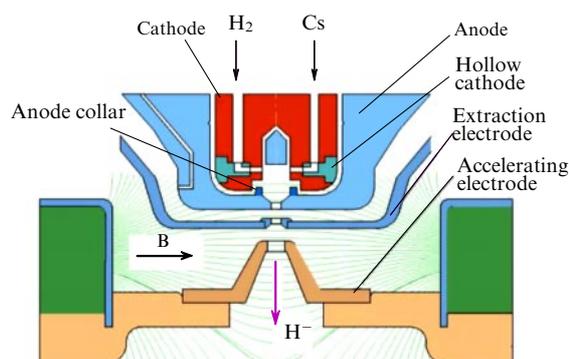
Figure 3. (Color online.) Schematic of a stationary Penning ion source with plasma injection from hollow cathodes (section along the magnetic field lines).

with an independent emitter be used. Simultaneously, the development of a surface-plasma source with the Penning geometry of the gas-discharge chamber and massive cooled electrodes was undertaken. In 2002, stable generation of a stationary beam with a current of 5 mA was achieved using this source [51], and it was installed on the tandem accelerator [52].

A schematic diagram of the Penning surface-plasma source of negative ions with plasma injection from hollow cathodes [53] is presented in Fig. 3.

Hollow cathodes used to inject the plasma into a Penning discharge are made in the form of small cylindrical inserts into massive cathode protrusions. Hydrogen and cesium are fed into the discharge through cathode cavities with small exit holes 1.2 mm in diameter. A compact external cesium furnace with cesium chromate-titanium pellets is used to supply cesium. Plasma emission from cathode cavities maintains a stationary Penning discharge with currents up to 10 A and a voltage of 70–120 V at a reduced hydrogen pressure in the gas discharge chamber (4–5 Pa). For a quick start, the source is heated by inbuilt ohmic heaters.

Negative ions in the Penning source are formed due to the conversion of fast atoms on the cesium-coated anode surface. The anode coating with cesium, optimal for generating
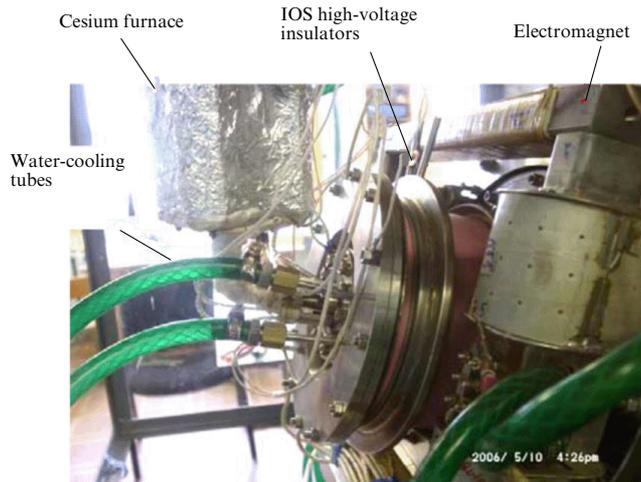
Figure 4. (Color online.) First stationary Penning ion source designed for the tandem accelerator.

Figure 5. (Color online.) Contour diagram of emittance of a negative ion beam with 15-mA current.

negative ions, can be maintained under conditions of a stationary Penning discharge with a current of 7–10 A at an anode operating temperature of $250-300\,^\circ$C. The extraction and acceleration of the beam are performed using a three-electrode ion-optical system (IOS). The magnetic field of ~ 0.1 T needed for maintaining the Penning discharge and separating the beam of negative ions from the co-streaming electrons in the experimental source is generated by an external magnet. The source prototype on the test bench provided a stationary beam of H$^-$ ions with a current up to 8 mA and normalized emittance of ~ 0.7 mm mrad (for 90% of the beam with an energy of 23.5 keV) [53].

The design and characteristics of the Penning surface-plasma source of negative ions with hollow cathodes are described in detail in [54–56]. In 2006, this source was installed on the tandem accelerator (Fig. 4). Over the course of more than a decade of operation, several modifications have been made in its design to increase the service life and simplify the maintenance. The total time of work of the source in 2006–2018 was more than 3200 hours, with its average daily duration amounting to 5 hours. The general operational statistics of the source operation on the BINP tandem are presented in Ref. [56]. Using this source, a proton beam with a current of 6.7 mA and an energy of 2 MeV was obtained [57]. To produce negative ion beams with enhanced ion current and energy under conditions of long-term continuous operation, modified versions of the Penning source with hollow cathodes were developed [58, 59]. The ion source used in Ref. [58] made it possible to obtain stationary beams of H$^-$ ions with a current up to 15 mA, discharge current of 6–7 A, discharge voltage of 75–85 V, hydrogen supply of $0.15\,l\,$Torr s^{-1}, and magnetic field of ~ 0.1 T.

An XX'-diagram of a negative ion beam with a current of 15 mA and energy 30.7 keV that characterizes its angular divergence and emittance is presented in Fig. 5 showing closed curves containing 50%, 70%, and 90% of the beam current.

Root-mean-square 1 RMS emittance (RMS — root mean square) in the XX' phase plane is given by the expression $\varepsilon_{1\mathrm{RMS}} = \beta\gamma \left[\langle X^2 \rangle \langle X'^2 \rangle - \langle XX' \rangle^2 \right]^{1/2}$, where β, γ are relativistic factors, X is the transverse coordinate, and X' is the angle of inclination of the trajectory to the Z-axis (beam propagation direction) in the XZ plane. The angle brackets denote the mean values of quantities X^2, X'^2, and XX' determined
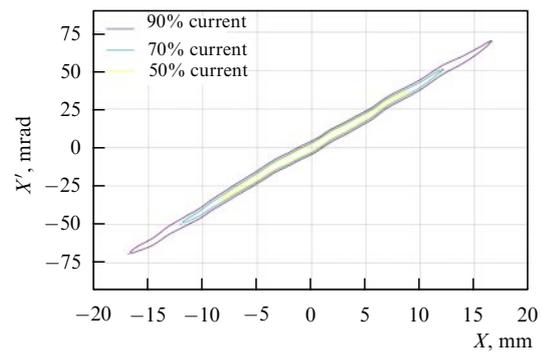
taking into consideration the distribution function of the beam particles in the phase plane XX'. The value of IRMS-beam emittance for the diagram shown in Fig. 5 is $\varepsilon_{1\mathrm{RMS}} \approx 0.2\pi$ mm mrad.

Later, the Penning surface-plasma source was modified to enhance the ion flux [60, 61] by increasing the diameter of emission holes in the anode and the ion-optical system up to 5 mm. Also, the magnetic system of the source was modified. To reduce the flow of electrons extracted from the plasma together with negative ions, a special protrusion was made through an enlarged hole in the near-anode region and around the emission hole (see Fig. 3). Due to the decrease in the flow of accompanying electrons, sputtering of the anode cover and erosion of the extraction electrode were reduced. These changes ensured the long-term operation of the ion source with a beam current of 25 mA, an emission current density of more than $0.125\,$A cm^{-2}, and a discharge current of ~ 10 A [61]. At a discharge current of more than 10 A, no saturation of the beam was observed. At present, it is planned to install the developed ion source with increased current at the BINP tandem accelerator.

In addition, a stationary recharge source of a beam of negative hydrogen ions with a current of ~ 10 mA is being developed to be used for injection into the BNCT tandem accelerator at BINP, where a beam of negative ions is created due to dissociation of the beam of primary molecular ions and subsequent recharging in the target from gaseous hydrogen. To obtain a primary beam with a high content of H$_2^+$ molecular ions, a plasma high-frequency (HF) emitter is used. An advantage of this approach is the reduced required power of HF discharge and a relatively low supply of hydrogen into the discharge compared with that in sources generating beams with a high proton content. Moreover, at such an energy, it is quite easy to obtain weakly diverging beams without the use of fine-structured grids and with reduced requirements for the accuracy of their production. The primary beam of hydrogen ions with a current of 1–2 A and an energy of 30 keV is formed by a multi-aperture four-electrode ion-optical system with ballistic focusing.

The thus formed beam of hydrogen ions then passes through the recharge hydrogen target. Molecular H$_2^+$ ions in the charge-exchange target dissociate into two protons, each with half the energy corresponding to the maximum yield of negative ions in hydrogen. After successive charge-exchange acts or direct double charge-exchange, protons with an energy of 15 keV form a beam of H$^-$ ions at the exit from the target. The resulting beam is deflected 90° by the focusing rotary

magnet and is thereafter accelerated by the one-aperture ion-optical system to the energy of 100 keV. The fast atom beam that passed the magnet and proton beams deflected by the magnet enter the inclined receivers intensely cooled by water. To reduce stripping of the negative ion beam, a high vacuum is maintained in the transport area by differential pumping out with the use of turbomolecular pumps. Presently, the designing of the ion source is completed and its constituent elements are being manufactured. The necessary feeding and control systems are ready for use.

2.2 Stripping target of the accelerator

To strip the negative ion beam after the initial phase of acceleration, an argon stripping target was installed on the high-voltage electrode made in the form of a 400-mm-long cooled tube with an inner diameter of 16 mm. The gas is injected into the middle of the target. For a negative hydrogen ion with an energy of 1 MeV, the cross sections for the processes of its interaction with argon atoms are given in the table [62].

Processes involving the capture of an electron at such energies can obviously be disregarded; then, the yield of negative ions (N^-), atoms (N^0), and protons (N^+) from the target can be written as

$$N^- = \exp\left[-(\sigma_{-10} + \sigma_{-11})\pi\right], \tag{1}$$

$$N^0 = \frac{\sigma_{-10}}{\sigma_{-10} + \sigma_{-11} - \sigma_{01}}\left\{\exp(-\sigma_{01}\pi)\right.$$
$$\left. - \exp\left[-(\sigma_{01}\pi + \sigma_{-11}\pi)\right]\right\}, \tag{2}$$

$$N^+ = 1 - \frac{\sigma_{-10}}{\sigma_{-10} + \sigma_{-11} - \sigma_{01}}\exp(-\sigma_{01}\pi)$$
$$+ \frac{\sigma_{-10}\sigma_{01} - \sigma_{-11}(\sigma_{-10} + \sigma_{-11} - \sigma_{01})}{(\sigma_{-10} + \sigma_{-11} - \sigma_{01})(\sigma_{-10} + \sigma_{-11})}$$
$$\times \exp\left[-(\sigma_{01}\pi + \sigma_{-11}\pi)\right], \tag{3}$$

where π is the target thickness.

The dependence of the charge composition of the beam on the line argon density in the target is illustrated in Fig. 6. To set the desired target thickness providing a 90% proton yield, a Faraday cup was used to measure the beam current at the accelerator output.

To this effect, the amount of the gas to be fed was selected so as to ensure the equality of the proton current at the output and the current of negative hydrogen ions at zero current at the Faraday cup. The calculated thickness of the target was 0.32×10^{16} cm^{-2}. The gas inlet was then increased by 5.3 times to ensure the required 90% conversion of the initial beam into protons [63].

The interaction of an intense beam with the target leads to its partial ionization [49, 64]. In a stripping target, a hydrogen ion with an energy of 1 MeV loses about 600 eV and, accordingly, ionizes ~ 8 argon atoms. The charge-exhanging of a negative hydrogen ion into a proton is also accompanied
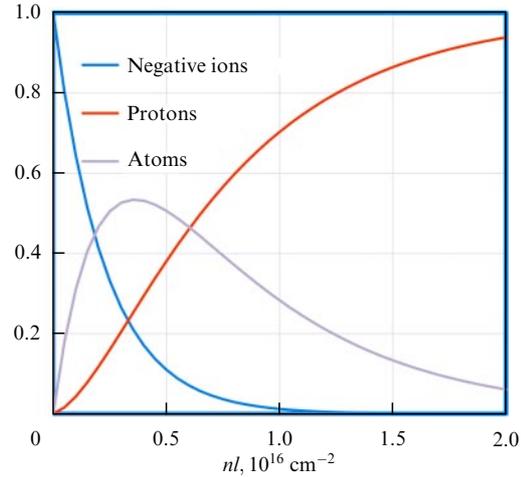
Figure 6. (Color online.) Fractions of beam components after passing through the stripping target.

by the appearance of two electrons with an energy of 500 eV that ionize about 10 argon atoms. Thus, the total number of ionizations K in the stripping target produced by one negative hydrogen ion is close to 18. At the characteristic beam current of 1 mA, $\sim 10^{17}$ argon ions are produced per second, which is many fewer than the gas puffing into the target ($\sim 10^{19}$ s^{-1}), and the resulting plasma is weakly ionized. The ionization rate of argon ions is dn_i/d$t \approx KI_b/(\pi a^2 L)$, where I_b is the beam current, a is the beam radius, and L is the target length. The ions are neutralized on the target walls at a rate of n_i/τ_i. In this case, the mean time of flight of ions to the wall τ_i can be estimated as $\tau_i \approx a/V_i$, where V_i is the velocity of argon ions in the target.

Because electrons are more mobile than ions, the plasma in the stripping target must have a positive potential with respect to the wall if quasi-neutrality is to be maintained. Let us assume the temperature of electrons in the secondary plasma to be 5 eV. Then, taking into consideration that the plasma potential in the target is approximately three electron temperatures, the potential can be estimated as ~ 15 eV. This allows estimating the energy of argon ions in the target at ~ 15 eV. Hence, $V_i \sim 5 \times 10^5$ cm s^{-1}.

As a result, the equilibrium density of argon ions in the target will be $n_i \approx KI_b/(\pi a L V_i) \approx 3 \times 10^{10}$ cm^{-3}. Under the action of this potential, some of the positive argon ions leave the recharge tube and enter accelerating channels for negative hydrogen ions and protons. In these channels, argon ions are accelerated to 1 MeV and undergo defocusing by the input or output lens of the accelerator.

Taking account of the solid angle at which the hole in the accelerating channel is visible, it can be found that the current of ions from the target to the end face into the electrode system of the accelerator $I_{Ar} \approx 2\pi a^2 n_i V_i b^2/s^2 \approx 40$ μA, where b is the radius of the channel, and s is the distance between the target end and the first electrode. Argon ions accelerated to an energy of ~ 1 MeV hit the walls of the accelerating channel and cause fluxes of secondary electrons,

Table. Cross sections of processes of interaction of a hydrogen ion with argon atoms

σ_{-10}, cm^2	σ_{01}, cm^2	σ_{-11}, cm^2	σ_{0-1}, cm^2	σ_{10}, cm^2	σ_{1-1}, cm^2	$F_{+\infty}$, %
4.2×10^{-16}	1.6×10^{-16}	0.22×10^{-16}	6×10^{-21}	8×10^{-20}	1.7×10^{-24}	99.988

which can account for a significant fraction of the beam current. In addition, the interaction of the beam with the target leads to the excitation of argon atoms with the emission of photons with an energy of 10–15 eV. The number of excited F atoms per beam particle can be estimated as $F \sim 30$. At a beam current of 1 mA, the photon flux into accelerating gaps can be estimated at $\sim 5 \times 10^{15}$ s^{-1}. Assuming the coefficient of secondary emission of these photons to be 0.1, we find that a current of secondary electrons of ~ 80 µA is generated in the gaps of the accelerator. Photons have sufficiently large reflection coefficients (~ 0.6) and can fall on ceramic insulators between the electrodes, causing breakdowns. Summing up the above, it can be concluded that the flows of secondary particles in the accelerator can be considerable, and it is necessary to take all measures to suppress them.

The interaction of the beam with the gas and plasma in the target leads to the angular spread and some deceleration of the beam. The stopping power and scattering cross section of a proton with an energy of 1 MeV are given, for example, in Ref. [65]. According to [65], the loss in beam energy for a target as thick as 2×10^{16} cm^{-2} is ~ 400 eV, and the energy spread resulting from the interaction with the target can be ignored. The same refers to the emerging angular spread, taking into account its smallness ($\sim 4 \times 10^{-3}$ mrad) compared with the angular spread of the beam at the target entrance.

The presence of plasma in the target can, in principle, result in beam-plasma instability that also causes beam scattering. The instability increment $\gamma \approx 0.7(n_{\text{beam}}/n_{\text{plasma}})^{1/3}\omega_{\text{pe}}$ in the case of a beam current of 10 mA is $\sim 1.5 \times 10^5$ s^{-1}. Collisions of plasma electrons with argon atoms in the target stabilize the beam-plasma instability, because their frequency is higher than the instability growth rate. An additional stabilizing factor is the inhomogeneity of the beam being converted and of the secondary plasma along the target. For this reason, beam scattering and deceleration in the conversion target can be disregarded.

2.3 Lithium target for neutron generation
A solid lithium target has been used to generate neutrons [66]. To obtain a lithium layer of the desired thickness, vacuum deposition from the vapor phase on the substrate was used. The substrate was intensively cooled to maintain the lithium layer in the solid state during its heating by a powerful proton beam [67]. The substrate temperature was controlled during the deposition.

The thickness of the lithium layer was determined by measuring electrical conductivity of distilled water into which the lithium-coated target was placed [68]. The target thickness could also be determined from the intensity of photons with an energy of 478 keV emerging in the ^{7}Li(p, p$'\gamma$)^{7}Li reaction when the proton beam scanned the target surface [69]. The measurements showed that the density of the sputtered lithium corresponds to that of solid Li. Using secondary ion mass spectrometry, it was found that the purity of the lithium layer and its stability with respect to the residual gas in the accelerator are sufficient for efficacious neutron generation [70].

The deposited lithium layer had a thickness necessary to slow down protons to the neutron generation threshold of 1.882 MeV, making it possible to reduce the accompanying γ-ray flux with an energy of 0.478 MeV and lithium temperature.

In order to correctly choose the materials used to construct the target, the dose rate and the spectrum of γ-radiation, as well as the dose rate of neutron radiation and the emission spectrum from residual activity during irradiation with 2-MeV protons of various structural materials, were measured [71]. The cross section of the reaction ^{7}Li(p, p$'\gamma$)^{7}Li was measured at proton energies from 0.7 to 1.85 MeV; also, the yield of photons with an energy of 478 keV from the thick lithium target was measured for the first time [72]. It was found that a decrease in lithium thickness from 300 to 60 µm at a proton energy of 2.3 MeV leads to a 1.9-fold decrease in the dose of unwanted γ-radiation without a change in the neutron yield [73].

Using a CCD (charge-coupled device) camera and a remote microscope, *in situ* blistering was observed when copper and tantalum were irradiated with 2-MeV protons [74]. It has been found that the threshold for the formation of blisters on the copper surface depends on the purity of the copper. For example, for ultrapure copper, it turned out to be 3×10^{19} cm^{-2} at approximately 150 °C; it was one seventh that for ordinary copper. In the case of tantalum at a fluence of 3.6×10^{20} cm^{-2}, the surface is modified with the formation of a relief having the characteristic cell size of ~ 1 µm, and the formation of blisters at a substrate temperature of 160–200 °C occurs at a fluence exceeding 6.7×10^{20} cm^{-2}.

It has been shown that the formation of blisters on the copper surface does not lead to a decrease in the neutron yield, and the target can continue to be used for neutron generation.

2.4 Beam scanning
The use of magnetic sweep of a proton beam [75] provides the desired profile of beam current density at the target, which guarantees the absence of local overheating to a temperature exceeding the melting temperature of the lithium layer. A beam with a diameter of around 2.5 cm unfolds along the helical trajectory with a constant azimuthal velocity, which ensures a more uniform target exposure. The sweep has four current windings placed in a box-shaped magnetic circuit with an internal square opening for the beam to pass through. Sinusoidal currents in the windings are generated using pulse-width modulation.

The sweep is carried out by shifting the phases of the current in pairs of opposite windings by 90°. The beam is swept by a near-uniform magnetic field with a strength up to 500 G rotating at a frequency of 100–2000 Hz. Scanning along the radius occurs at a frequency of 1–10 Hz.

2.5 Beam diagnostics in a tandem accelerator
A tandem accelerator is equipped with diagnostic tools for determining the characteristics and position of a beam and for detecting gamma radiation and neutrons. To measure the energy of the proton beam, a resistive divider connected directly to the high-voltage electrode of the tandem is used. The divider is located in a tank filled with SF$_6$, inside the secondary circuit of the rectifier, and is connected at one end to the high-voltage electrode of the source and at the other end to the 'earth' electrode. There are no intermediate connection points of the divider with the construction elements. The divider was calibrated by measuring the voltage dependence of the neutron dose rate that appeared when the proton energy threshold of 1.882 MeV was exceeded in the ^{7}Li(p, n)^{7}Be reaction. The threshold reaction for the generation of monochromatic resonant γ-quanta with an energy of 9.17 MeV in the reaction ^{13}C(p, γ)^{14}N was also used. Gamma ray quanta were generated at a resonant proton
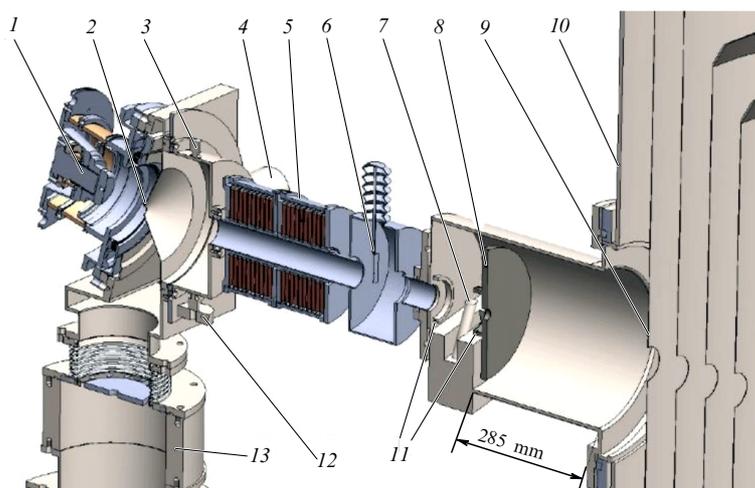
Figure 7. (Color online.) Low-energy beam path: *1* — ion source, *2* — conical diaphragm, *3* — vacuum sensor, *4*, *13* — turbomolecular pumps, *5* — magnetic lens, *6* — movable diaphragm, *7* — OWS-30 scanner, *8* — cooled diaphragm, *9* — first electrode of the accelerator, *10* — vacuum volume, *11* — ring electrodes for blocking secondary emission, *12* — leak.

energy of 1.746 MeV [76], with the width of the resonance level of the ^{14}N nucleus being only 128 eV [77, 78]. Owing to the small width of proton capture resonance, the slope of the recorded excitation curve of this spectral line was determined by the spread of the proton energy in the beam, which made it possible to measure the beam energy spread with high accuracy. The measured energy spread at an energy of 1.75 MeV was 1.2 ± 0.15 keV at a beam current of 1.5 mA [79].

To register γ-radiation arising from the beam–target interaction, we used a detector based on a 6-cm-long NaI crystal 6 cm in diameter and a Photonis XP3312V photomultiplier. The photomultiplier signal was recorded by a high-speed spectrometric analog-to-digital converter. The detector was located at a distance of about 2 m from the target. The rectangular inlet of the collimator was 10×15 cm in size [80]. Also used were NaI- and BGO-gamma spectrometers, as well as an SEG-1KP gamma-ray spectrometer. A semiconductor detector made from highly pure germanium at the Institute of Physical and Technical Problems (Dubna) was used to measure the flux and spectrum of gamma radiation.

To measure the power of the beam incident on the target, the temperature of the cooling water was measured upon entering and exiting the target. The oil temperature in the cooling system of the stripping target was also measured, which made it possible to determine the power release from the proton beam on it.

The neutron flux was measured using BDT (Bubble Detector Thermal) and BD100R (Bubble Technology Industries, Canada) bubble detectors. The former device has the highest sensitivity in the range of thermal neutron energies, and the latter one is more sensitive to neutrons with an energy of ~ 100 keV. For remote measurements of the neutron flux, we used a GS20 lithium-containing scintillator (Saint-Gobain Crystals, USA) mounted on a Hamamatsu R6095 photomultiplier with an MHV12-1.5K1300P high-voltage power supply (TRA CO Electronics, Japan). An SWX-1552 activation foil set (Shieldwerx, USA) was used to measure the neutron spectrum.

The magnitude of the dark current between the tandem electrodes was determined from the difference between the readings of two dividers connected to the high-voltage

electrode. One of them was used to measure the beam energy (see above) and the other to set potentials at the tandem electrodes [81]. The second divider was placed in an SF$_6$ gas, and its connecting elements were fixed on the electrodes of both the vacuum and gas parts of the bushing insulator. In the absence of dark currents, the currents of both dividers coincided. When dark currents appeared, a difference arose, from which it was possible to directly determine the current in the gap between the vacuum tank and the first accelerating electrode. The dark current in other accelerating gaps was not measured directly; it could be estimated on the assumption of equality of dark currents in all gaps.

An OWS-30 scanner (beam profile meter) manufactured by D-pace (Canada) was used to measure the profile, position, and current of a beam of negative hydrogen ions in real time. The position of the scanner is shown in Fig. 7. The beam current was measured by a NPCT-CF4"1/2-47.7-120-UHV noncontact current sensor (Bergoz Instrumentation, France) in the 8-kHz band (not shown in the figure). The scanner, in combination with the movable diaphragm *6*, was used to control *in situ* negative ion beam emittance [82]. To block secondary emission from the scanner wires, a negative bias was applied to the ring electrodes *11*.

The position and size of the ion beam were monitored using Hikvision video cameras aimed at the input and output diaphragms of the accelerating electrode, recording visible radiation caused by ionization of the residual and stripping gas by ions [83]. The beam current and its position were determined using movable Faraday cups at various sections along the beam.

The lithium target unit used for neutron generation was electrically isolated, which made it possible to apply short high-voltage pulses to it to measure the neutron spectrum with the use of the time-of-flight technique when operating in the neutron threshold generation mode. The accelerator operated at a proton beam energy below the reaction threshold ^{7}Li(p, n)^{7}Be (1.882 MeV). When a negative short (200 ns) voltage pulse of 45 kV was applied to the neutron-generating target, the proton energy increased to 1.915 MeV, which led to a burst of neutron radiation. Rectangular high-voltage pulses were created using a double forming line and a

thyratron operating as a key with a frequency up to 250 Hz. Neutrons were registered by a remote detector consisting of a lithium-containing GS20 scintillator (4 mm thick, 18 mm in diameter) and a photomultiplier. The time of flight of neutrons was determined by a VCP-1 digital time-converter: the time interval between the moments when high voltage was applied to the target and the appearance of a signal from the neutron detector was measured [84].

Electrical insulation of the target also made it possible to measure the beam current directed straight to the target. The current-voltage characteristic of the target was determined. When a small positive bias was applied to the target, the current to it coincided with good accuracy with the beam current measured by a movable Faraday cylinder.

The position and size of the proton beam on the surface of the lithium target were controlled by eight thermocouples inserted from the end face into holes in the copper substrate of the target. Also used for this purpose was a Flir T650sc thermal imager (USA) mounted on a bending magnet branch pipe with a barium fluoride window. The state of the target surface was monitored *in situ* with a Hikvision video camera through a nozzle with fused silica glass.

Flir T650sc (FLIR Systems Inc., USA) and Optris PI 640 (Germany) infrared cameras (thermal imagers) were used to study the processes of heating internal elements of the accelerator and the neutron-generating target.

A KX InfiniMax™ long-focus microscope (Infinity Photo-optical Co., USA) was used to observe target blistering under proton beam irradiation. An RGA300 gas analyzer (Stanford Research Systems, USA) served to determine the composition of the residual gas inside the vacuum chamber of the accelerator.

For the dosimetry of ionizing radiation and to ensure the radiation safety of personnel, the following equipment was used: a DKS-96 dosimeter-radiometer with BDMN-96 and BDMG-96 detection units (Doza Ltd., Russia), a DBG-S11D gamma radiation dosimeter, a UDMN-100 device for neutron detection, and a BOP-1M data processing and transmission unit (Doza Ltd., Russia), as well as spherical ionization chambers and gamma detectors with a Micro Gamma LB 112 display unit (Berthold Technologies, Germany). The equivalent dose rate of neutron radiation in the accelerator bunker was measured by a BDMN-100-07 detection unit (Doza Ltd.) consisting of a spherical moderator with a UDMN-100 detection unit located in it. The detection unit was mounted on the wall of a radiation-protected room at a distance of 3.6 m from the target at an angle of 34° to the direction of the proton beam. The dose rate measurement error was 25%. An RZB-05D-01 radiometric unit was used to ensure the radiation safety of personnel during work with open sources of ionizing radiation.

3. Main results of studies on the neutron generator prototype (2009–2020)

3.1 Investigations into physical processes in the accelerator

The tandem accelerator design used has a specific problem associated with the relatively large energy (on the order of several ten joules) stored in the capacitances of the nested electrodes of the system due to their large area. During breakdowns, the release of the stored energy can lead to damage of the electrode surface and deterioration of the high-
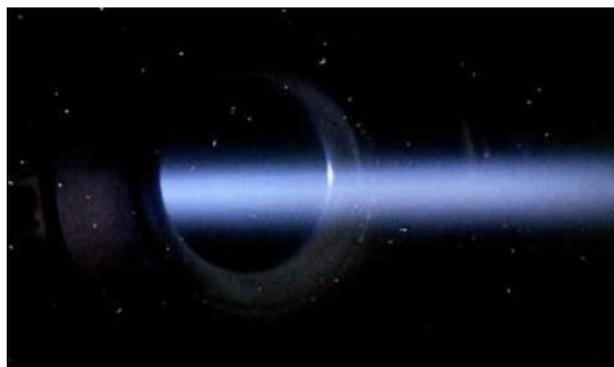
Figure 8. (Color online.) Beam image taken with a video camera at a proton current of 9 mA.

voltage strength. Nevertheless, experiments have shown that breakdowns with energies up to 50 J do not significantly affect the surface, nor do they reduce the high-voltage strength of the embedded electrodes, and the dark current is acceptably low at an electric field strength on the electrodes up to 60 kV cm^{-1} [37]. Possible sources of dark current were identified and the design of the accelerator optimized so as to reduce the local electric field strength in these places to an acceptable level. For high-voltage simulation exercises on the accelerator, a special computer algorithm was developed, which is automatically implemented if necessary [85, 86].

Experiments showed that a space charge markedly affected focusing of the beam in the low-energy path, its shape, and losses in the accelerator. The dependence of the beam profile of negative hydrogen ions on the residual gas pressure was measured. The beam profile was determined with a wire scanner, while the beam phase diagram was measured with a scanner, as was the movable diaphragm in front of it [87]. The influence of the space charge and of spherical aberration of the focusing magnetic lenses on the ion beam was documented. It was shown that the beam has a round shape (Fig. 8), and the maximum density of its current is reached at an intermediate pressure in the transport channel.

The flow of secondary charged particles leaving the accelerator was also studied [88, 89]. The experiments demonstrated that the majority of secondary particles are formed as a result of beam-induced ionization of the residual gas in the gaps between the electrodes and the gas in the stripping target. Furthermore, an important role is played by secondary electron emission from the walls of the beam path during irradiation with high-energy argon ions formed in the stripping target as a result of interaction with the beam. Data on the coefficient of secondary electron emission K for argon ions in various materials at an energy of ~ 1 MeV are presented in [90]. According to Ref. [90], $K \geqslant 10$ at normal incidence and the energy of argon ions $E \geqslant 1$ MeV. The coefficient further increases in the case of oblique incidence and the presence of gas layers on the surface [91, 92]. Taking these facts into consideration, measures were implemented to suppress electron emission from the end walls of the accelerator. They included the installation of cooled diaphragms at the input and output of the tandem, in front of which grids were placed under a negative potential to suppress electron emission. These measures, combined with an increase in the pumping rate at the input/output of the accelerator, made it possible to reduce the current of
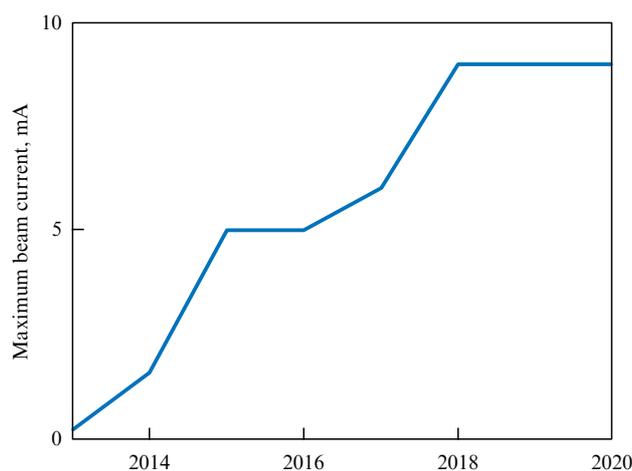
Figure 9. Maximum beam current in the accelerator.

secondary particles from 60% of the ion beam current to less than 8% [93].

Taken together, the conducted research and modernization of the accelerator allowed the proton beam current to be increased from 100 µA during initial commissioning [94] to 1.6 mA after optimization of ion beam injection into the stripping target [95]. Thereafter, the beam current was increased to 5 mA following suppression of secondary charged particles [89]. After careful adjustment and optimization of the ion beam size at the accelerator input, the current was increased to 7 mA and then to 9 mA. Presently, beam losses in the accelerator are minimized, and the current of the proton beam is limited by the current of negative hydrogen ions from the ion source.

Figure 9 shows the change in the maximum current of the accelerated beam in the tandem accelerator during its commissioning and modernization.

At the initial stage, in 2006–2013, work was carried out at a beam current of 0.05–0.2 mA [94]. The stable operation of the tandem accelerator at a current of 1.6 mA [95] was achieved by removing the uncooled diaphragm at the accelerator inlet that emitted electrons during heating, which led to breakdowns. The position of the beam at the entrance to the accelerator was monitored using a video camera. Simultaneously with increasing the current, it was possible to improve the vacuum in the installation and reduce the X-ray dose rate during the operation of the accelerator.

A further increase in the beam current [88, 93] to 5 mA resulted from the reduction of the fluxes of secondary electrons knocked out from the walls of the beam path by accelerated argon ions from the stripping target of the accelerator. For this purpose, cooled diaphragms were installed at the input and output of the accelerator, the secondary emission from which was suppressed using grid electrodes. Also, a diaphragm was placed at the entrance to the accelerator to which a negative bias was applied. It served to block secondary electrons formed in the path of the low-energy beam during stripping of negative ions and ionization of the residual gas.

An increase in beam current to 6 mA [87] was achieved by virtue of more precise control of the size and position of the beam using a wire sensor installed at the entrance to the accelerator. The measurements performed made it possible to reveal the noticeable influence of the space charge on the beam size and to correct the beam focusing before entering the accelerator to compensate for this effect. Subsequently, the beam current was increased to 7 mA [96] and further to 9 mA with more careful control of the beam position in the accelerating path by means of optical diagnostics. The current of the negative ion beam at the input to the accelerator was ~ 10 mA. Apparently, some error in the measurement of the proton beam current was introduced by incompletely stripping the negative ion beam in the gas target.

After acceleration, the proton beam was transported to the lithium target located approximately 5 m from the accelerator. The position of the beam in the high-energy path was controlled by a set of magnetic correctors. The proton beam had a diameter of about 10 mm [97] at the exit from the accelerator and about 30 mm at the target. The diameter of the proton beam at the output was practically independent of the current, which suggests the absence of the space charge effect during its transportation in the high-energy path.

3.2 Studies on neutron generation

As was pointed out in Section 2.3, irradiation of a neutron-generating target with protons leads to blistering, i.e., bubble formation (Fig. 10), in copper and tantalum substrates. After the appearance of blisters, further irradiation does not lead to a change in the surface, probably due to the appearance of holes and cracks during blister formation. Samples obtained by four different methods for the deposition of tantalum on copper (explosion welding, diffusion welding, soldering, and plasma-arc deposition of tantalum and copper powders) are mechanically resistant to stationary and pulsed thermal loading up to 1 kW cm^{-2}. It was found in experiments that the surface temperature of tantalum rises during long-term irradiation. Apparently, this effect is associated with a decrease in thermal conductivity due to blister formation in the crystalline structure of the substrate.

The results of research made possible the development of a three-layer lithium target consisting of a thin layer of pure lithium, a thin layer of a material resistant to the formation of radiation blisters for proton absorption, and a copper substrate for efficient heat removal. Such a design provides a stable neutron yield with an extended target lifetime [98].

To obtain a neutron beam suitable for clinical use, a special shaper (BSA) was developed. The shaper consists of a moderator, a reflector, an absorber, and filters. A composite moderator (magnesium fluoride near the target for neutron production and aluminum fluoride close to the outlet) and a composite reflector (graphite in the front hemisphere and lead in the back one) are used. Numerical simulation showed that this approach provides the required spectrum of neutrons and accompanying gamma radiation in the ^{7}Li(p, n)^{7}Be reaction at a proton beam energy of 2.3 MeV [98, 99].
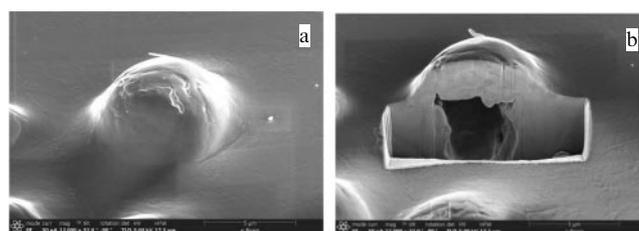
Figure 10. (a, b) Images of the surface of 99.996% copper obtained with an FIB-SEM Helios G3 UC electron microscope. Figure b shows a blister specially cut by the ion beam.
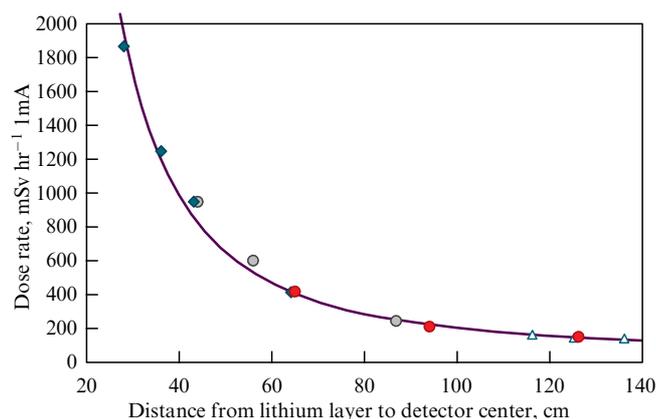
Figure 11. Dependence of dose rate on distance from the lithium target along the direction of the proton beam.

The $^7\mathrm{Li}(\mathrm{p, n})^7\mathrm{Be}$ reaction is accompanied by the accumulation of radioactive isotope $^7\mathrm{Be}$ in the lithium layer. A special study showed that almost all radioactive beryllium remains in the lithium layer during operation of the neutron source. The $^7\mathrm{Be}$ isotope has a half-life of 53.3 days, which requires special handling and storage of lithium targets. The targets used were placed in a protected buried container for the period necessary for their cooling [100].

The integral neutron yield was determined from the intensity of gamma radiation in the $^7\mathrm{Be}$ target. The measurements were carried out using a γ-spectrometer with an NaI scintillator. The neutron spectrum was measured by the time-of-flight method during the generation of short pulses of neutron radiation [101]. For this purpose, a compact neutron detector with a cast boron-enriched polystyrene-based scintillator was developed [102], which permits characterizing a thermal neutron flux [103].

The spatial distribution of the neutron radiation dose rate was determined using a DKS-96 dosimeter-radiometer with a BDMN-96 detection unit manufactured by the Doza Research and Production Enterprise. Results of the measurement at a proton beam energy of 2 MeV are presented in Fig. 11 (different symbols indicate values obtained on different days).

The dose rate normalized to a beam current of 1 mA decreased with increasing distance z as $D = 1500/z^2 + 0.05$, where D is the dose rate in Sv h^{-1}. The constant term in this dependence originates from the contribution of scattered neutrons. Apparently, the dose rate is somewhat overestimated due to the relatively soft neutron spectrum and the resulting high dosimeter readings. Measurements of the angular distribution of the dose rate confirmed the direction of the neutron flux: the dose rate decreased by a factor of 2.7 when measured at an angle of 90°. The measured dose rate of the accompanying gamma radiation was roughly 60 times lower.

3.3 *In vitro* medico-biological research and other applications of the neutron source

Experiments were designed to elucidate the effect of neutron irradiation on the viability of human tumor cells. We used the U87 human glioblastoma cell line representing a line of human tumor cells of glioma origin well suited to the goals of BNCT of diffuse brain tumors and a cell line of mouse fibroblasts. *In vitro* studies were carried out using boronphe-nylalanine enriched with the boron-10 isotope in the optically isomeric form L. A phantom simulating the structure of the human head was used in the experiments. Cell samples were placed in front of and behind the perspex phantom. The samples positioned in front of the phantom were under conditions similar to those taking place when the patient's skin is irradiated with fast and thermal neutrons and γ-radiation. Experiments with the human glioblastoma cell line U87 showed that, with the integral operation of the accelerator corresponding to 1 mA h, no significant changes in cell viability were apparent in any sample during several days. Significant changes in cell viability developed after two weeks, when almost all boron-containing cells were destroyed [104, 105]. A clonogenic analysis of cell structures after irradiation was undertaken in Ref. [106]. It demonstrated a markedly enhanced cytopathic effect of a slow neutron beam in the presence of boronphenylalanine [107]. Currently, experiments continue on laboratory animals.

The developed neutron generator based on the tandem accelerator with a vacuum insulation also finds other applications besides the generation of epithermal neutrons for BNCT. For example, it has been recently used to measure the content of hazardous impurities in boron carbide samples obtained for the international thermonuclear experimental reactor (ITER) [108].

It is planned to use the neutron source for radiation testing of calibration system fibers of the laser calorimeter of the CMS (Compact Muon Solenoid) electromagnetic detector developed for the Large Hadron Collider at CERN [109, 110]. To generate fast neutrons, hydrogen in the ion source was replaced by deuterium, and a deuteron beam with an energy of 2 MeV and a current of 1.1 mA was used to generate neutrons with an energy of 5.7 MeV. In this case, the neutron yield was 1.4×10^{12} s^{-1} [111].

The use of a special target ($^{13}\mathrm{C}$) makes it possible to generate a stream of monochromatic γ-quanta for the urgent detection of explosives and narcotic substances [112], and α-particles for the study of promising neutronless thermonuclear synthesis of $^{11}\mathrm{B}(\mathrm{p},\alpha)\alpha\alpha$ [113] and positrons using the $^{19}\mathrm{F}(\mathrm{p},\alpha\mathrm{e}^+\mathrm{e}^-)^{16}\mathrm{O}$ [114].

Work on improving the design of the accelerator goes on continuously. To reduce its dimensions and increase stability of the potential distribution between electrodes, it was proposed to place a high-voltage rectifier inside the bushing insulator [115]. The possibility of rotation of the BSA or its moderator-containing part relative to the proton beam propagation axis can make it possible to direct neutrons to a patient's body at an angle and thereby enhance the efficiency of therapy of a concrete tumor [116, 117]. A method was proposed for obtaining a neutron beam exclusively in the epithermal energy range [118]. The beam may contain neutrons emitted at a certain angle towards the backward hemisphere when the proper choice of proton energy and given thickness of the lithium layer is made [119].

4. Neutron source for clinical trials of boron neutron capture therapy

The extensive experience in operating the experimental setup described in Section 3 made it possible to propose the concept of a new generation commercial neutron generator for BNCT under clinical conditions. Its layout is shown in Fig. 12.

Based on this concept, a neutron source was built and launched to conduct clinical trials of BNCT. Its features as
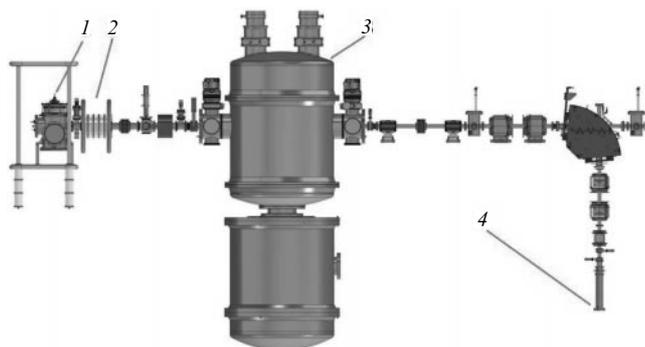
Figure 12. Concept of a neutron generator for clinical trials of BNCT. *1* — ion source, *2* — pre-accelerator, *3* — accelerator, *4* — neutron generating target.

well as individual results obtained at the initial stage of experimenting are discussed below.

4.1 Source of accelerating voltage

The source of accelerating voltage in the tandem accelerator for BNCT is the modified rectifier of an ELV-type electron accelerator [120]. As discussed in Section 3.3, the rectifier in the accelerator prototype is connected to the tandem via the sectioned high-voltage feeder. The rectifier voltage is evenly distributed over the electrodes of the feeder and tandem by a high-resistance divider. However, the precipitation of charged particles onto the tandem electrodes upon beam acceleration can disturb the uniformity of the voltage distribution between the electrodes and result in breakdowns.

In the final version of the accelerator, the tandem electrodes are directly connected to rectifier sections using a bushing insulator. One part of it is located inside the tandem, the other is inside the high-voltage rectifier column, which ensures the connection of the rectifier sections with the intermediate electrodes of the tandem. This change required significant modification of the rectifier (Fig. 13).

The primary winding outside the column of rectifier sections is fed by alternating voltage with a frequency of 1400 Hz. Reverse-flow magnetic circuits are installed outside the primary winding, the diameter of which is greater than that in the standard ELV prototype.

The column from 18 rectifier sections mounted on a textolite plate is attached to the lower magnetic circuit with insulating rods. The sections made according to the voltage quadrupling scheme are connected in series. The maximum rectified voltage of each section is 80 kV; the load current amounts to 20 mA. The design of the rectifier sections is similar to that of a standard ELV section. SF_6 is used as the insulating gas. The rated output voltage of the rectifier is 1.2 MV.

To measure the accelerating voltage that does not exceed 1.5 MV, a divider from high-ohmic resistors was used in the ELV. At a voltage of 2.5 MV, a rotary voltmeter was used. The electric field along a column with this arrangement of the rectifier was approximately twice as high as in a standard ELV, which means that the divider from high-ohmic resistors failed to ensure the required reliability. Replacing the divider with a rotary voltmeter resolved the problem.

Modification of the high-voltage source makes it possible to reduce the height of the accelerator and, accordingly, the required ceiling height of the room where it is located. Moreover, when the electrodes are connected directly to rectifier sections, better stability of the potentials of the

Figure 13. (Color online.) High voltage rectifier.

intermediate electrodes is provided than that in the connection circuit with the ohmic divider used at the initial stage of the prototype operation. The rise in the nominal beam energy to 2.5 MeV is due to the rapid increase in the total neutron yield from the target when the beam decelerates as it passes through the large resonance of the $^7Li(p, n)^7Be$ reaction centered at an energy of 2.2 MeV. This provides a balance between the required proton current, the duration of therapy, and the quality of the beam (with a small fraction of fast neutrons).

To ensure stability of focusing and acceleration of the ion beam in the upgraded version of the tandem accelerator, the potential of the intermediate electrodes is set directly from the rectifier sections rather than with the use of the ohmic divider [120]. For this purpose, the rectifier was rotated 180° with respect to its position in the original design. The modified design of the rectifier made it possible to apply a potential to the intermediate electrodes of the accelerator directly from its respective sections, which reduced the effect of dark currents and transients on the stability of the accelerating voltage.

4.2 Negative ion source

Despite the advantages of the Penning surface-plasma source of negative ions described in Section 2, the operation of such a source under clinical conditions encounters difficulties. As an alternative, it was proposed to consider the possibility of using sources with volumetric formation of negative ions. In particular, the possibility of using a commercial source manufactured by D-Pace (New Zealand) was estimated. The design of this source was developed at the TRIUMF laboratory (Canada). The source provides generation of a beam of negative ions with an energy of 30 keV and a nominal beam current of 15 mA.

A D-Pace ion source is shown in Fig. 14. The plasma in it is generated by an arc discharge between heated tungsten cathodes and the wall of the source chamber that serves as the anode. A multipole magnetic field is created on the wall of the gas-discharge chamber by permanent magnets installed outside.
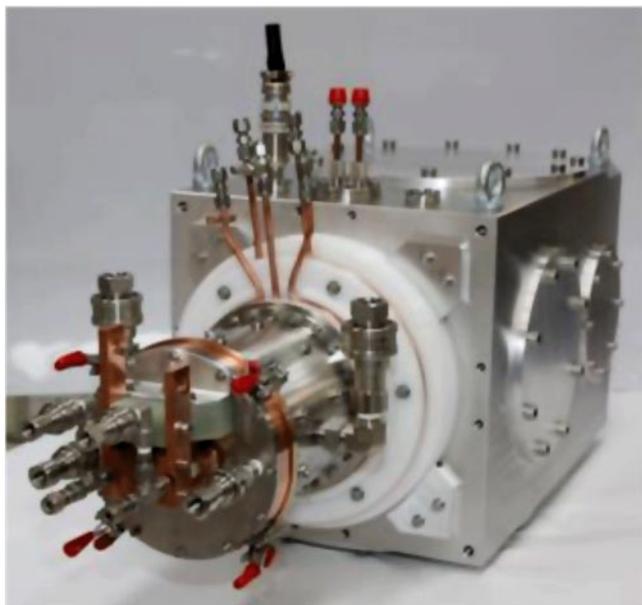
Figure 14. (Color online.) D-Pace ion source.

Figure 15. Dependence of the beam current measured by a Faraday cup from the arc current.

A peripheral magnetic field is used for the magnetic confinement of the plasma, increasing its density, improving the uniformity of the plasma discharge, and enhancing the ionization efficiency. Gaseous hydrogen is fed into the source to maintain the discharge and generate negative ions. A beam of negative H^- ions with an energy of 30 keV generated by this source can vary continuously within the range up to 15 mA with an emittance below 90 mm mrad.

The generation of negative ions in the source occurs as a result of a two-stage interaction:

$$H_2 + e\,(\varepsilon > 12\text{ eV}) \leftrightarrow H_2(v') + e + h\nu, \tag{4}$$

$$H_2(v') + e\,(\varepsilon < 2\text{ eV}) \rightarrow H^- + H. \tag{5}$$
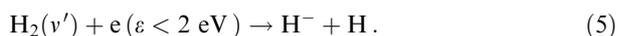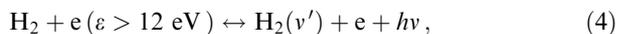
The key reaction leading to the formation of negative ions in the plasma volume is the dissociative attachment of an electron to a hydrogen molecule (5). The rate of this reaction is a complex function of the electron energy and the initial excitation of an electron characterized by the vibrational quantum number v'. The maximum yield of the dissociative addition reaction is achieved in a narrow range of quantum numbers v' that determines specific restrictions on electron energies for both stages of the interaction, (4) and (5). The population distribution of hydrogen vibrational levels and the electron energy distribution function can be controlled and tuned by adjusting parameters of the plasma discharge and changing the geometry of ion source electrodes.

The generation of negative ions in the volume makes it possible to continuously extract them from the plasma boundary. When negative ions are extracted from the plasma, the electrons simultaneously pulled out of the ion beam are deflected by a special magnetic filter. Then, the beam passes through magnetic correctors to be installed on the axis of the accelerator.

The ion beam is then transported to the diagnostic chamber, where a Faraday cup with an inlet diameter of 25 mm and a scanner are placed to measure the beam current and emittance, respectively. In what follows, results of the measurement of ion source parameters during extraction of
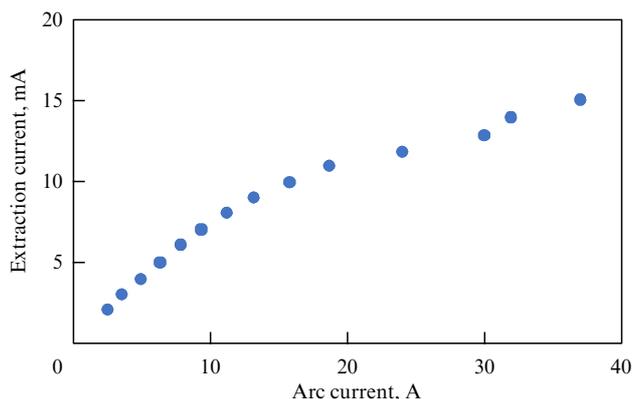
the ion beam are presented. The ion beam current varied in the range up to 15 mA with a step of 1 mA.

In this case, the pressure in the beam path behind the source was maintained at a level of $(1.2-4.6) \times 10^{-6}$ Torr. The gas intake varied from 12 to 28 standard cubic centimeters per minute (sccm) at the maximum values of the beam current. The gas efficiency of the ion source at a current of 10 mA was $\sim 0.5\%$. The dependence of the beam current measured by the Faraday cup on the discharge current is shown in Fig. 15.

The accompanying electron current for different exit holes exceeds the beam current by a factor of 2–5 at currents up to 10 mA. At higher currents, there is a tendency toward a rise in the relative current of the accompanying electrons.

4.3 Modernization of elements of the neutron source

The stripping target was modernized taking into consideration the experience gained during the operation of the neutron generator prototype. The target cooling system was optimized for better heat removal at the beam entrance and the walls of the target channel. The reduced number and length of joints in the pipelines for supplying the coolant to the target accounted for their enhanced conductivity and the pressure drop in the system. For better pumping of the target gas from a high-voltage electrode in which the target was installed, the design of the shutters in the tandem electrodes was changed in order to optimize their conductivity. This made it possible to increase the target diameter to 16 mm at a length of 423 mm and to improve the vacuum inside the electrode. The calculated beam diameter in the target center was $\leqslant 8$ mm, which ruled out the direct fall of beam particles on the target walls. To suppress the flow of argon ions from the target, special electrodes were used. Also, the possibility of precisely adjusting the target with respect to the accelerating channel was set out.

To absorb a beam accelerated to a high energy, a special receiver was developed. The beam receiver can be installed in the high-energy path of the accelerator after a 90-degree rotary magnet or a magnet that directs the beam into the room where the target is located. A beam receiver that can also be installed directly after the accelerator, e.g., for the period of launching a neutron source, is designed to correspond to the following beam parameters: energy of 2.5 MeV, current of 10 mA, beam diameter of ~ 1 cm.

The receiver that directly accepts the beam consists of water-cooled copper plates. The plates are inclined at an angle
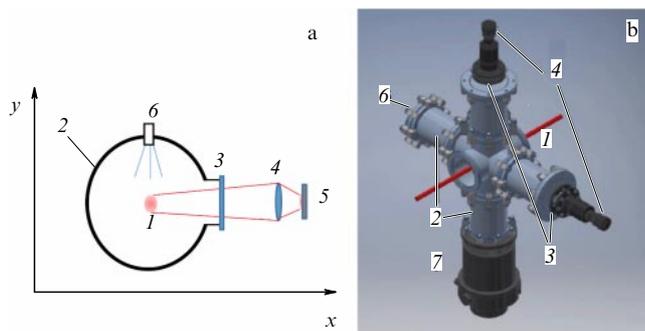
Figure 16. (Color online.) (a) Schematic of optical diagnostics of beam position and dimensions. (b) View of the diagnostic device: *1* — beam, *2* — vacuum chamber with blackened walls, *3* — optical window, *4* — lens, *5* — image registration unit, *6* — gas inlet, *7* — vacuum pump.

to the beam axis to reduce power density. It was assumed in the calculations that the allowable power density, taking into account the slope, should not exceed 2 kW cm^{-2}. To reduce the power density of the proton beam, a quadrupole magnetic lens with permanent magnets is placed in front of receiver plates.

To modernize the tandem accelerator, a current sensor of beam position has been developed. To determine the beam's position, four cylindrical water-cooled electrodes are used. When the beam is transported in the low- and high-energy paths, its size changes. Therefore, it is possible, if necessary, to move sensor electrodes along the radius, selecting the desired signal value. Measurements using the sensor allow determining not only the position of the beam but also its dimensions.

Moreover, optical diagnostics are used to control the position, size, and angular spread of a particle beam in the tandem accelerator [121]. The device and the setup for optical diagnostics are presented in Fig. 16.

In this diagnostic modality, radiation emitted by the beam's particles or the residual gas excited by the beam inside the vacuum chamber is used to determine the profile and position of the ion beam. In the past, such systems found application for diagnostics of powerful particle beams (see, for instance, Refs [122–125]).

The light emitted from the beam region is collected in the optical system through window *3* (see Fig. 16). To register the beam profile, a complementary metal oxide semiconductor sensor (CMOS camera *5*) is used. To increase the light-emitting ability, heavy gases are additionally let into the beam zone through valve *6*. Each channel of the CMOS matrix collects a beam of light along a chord crossing the

beam. The value of the signal on the detector channel with coordinate Y is proportional to the integrated beam density: $J(y) \propto \int n(x, y)\, dx$.

Observation from two different angles permits the position of the center of the beam and its profile to be determined. Basler AC1300NIR video cameras were used for registration. Light is collected by a lens with a focal length of 25 mm and relative aperture of 1.4. The focus of video cameras is adjusted by the lenses, allowing vertical and horizontal angle observations (see Fig. 16). The average blurring of a 10-mm segment along the survey chord due to the finite depth of field is estimated at 0.25 mm. To reduce the background scattered light, additional volumes *2* with a darkened surface were placed behind the beam in the field of view of the lenses. The distance from the central axis of the beam to the lenses is about 40 cm. The injected gas is pumped out by pump *7*.

Figure 17 shows measurement results for a beam with an energy of 35 keV. To increase the brightness of the beam glow, xenon was injected at a pressure of about 10^{-6} Torr, which led to the weakening of the beam by less than 1% due to the stripping on xenon atoms. The resulting image makes it possible to determine the position of the beam center depending on the longitudinal coordinate in the field of view (curve *1*), its inclination with respect to some chosen axis, and beam boundaries at half height (curves *2, 3*). A linear approximation of the dependence of the beam half-width on the longitudinal coordinate (Fig. 17b) makes it possible to determine the focusing/defocusing angle of the beam. In this case, as can be seen, the beam divergence angle is ~ 5.5 mrad. The accuracy of determining the position and width of the beam with a current of 10 mA and an energy of about 35 keV is about 0.1 mm at a relative tilt of the camera matrix and beam focusing of about 1 mrad.

Also, beam energy spread and angular divergence were measured. The accuracy of the energy spread measurement was roughly 100 eV for an angular divergence of about 3 mrad. The length of exposure was 50–100 ms. The acceptable accuracy (1 mm) of determining the position of the beam was reached in the case of a relatively short (less than 10 ms) impact on the beam with the pulsed gas supply to the beam path for enhancing the radiation intensity. The addition of the gas was accompanied by the stripping of negative ions; therefore, the amount of injected gas had to be optimized. The introduction of xenon was found to be especially effective and ensured an increase in the radiation intensity by a factor of ~ 40 compared with that in the case of hydrogen and by a factor of ~ 2.5 in the case of argon at a beam energy of about 35 keV. The exposure time at this beam
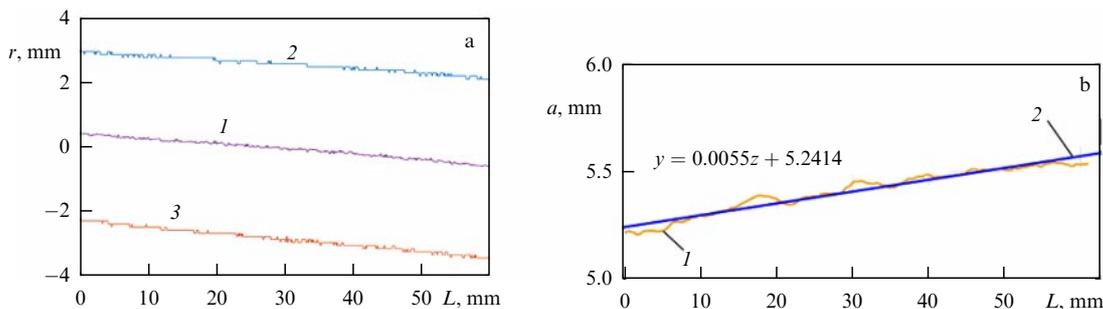
Figure 17. (a) Position of beam center of gravity (curve *1*) and its boundary at half-height (curves *2, 3*) along the transport channel. (b) Beam width at half-height depending on the longitudinal coordinate (curve *1*) and its linear approximation (curve *2*).

energy was less than 10 ms, and the position of the beam was measured with an accuracy of about 1 mm. The injection of xenon resulted in the loss of roughly 5% of the beam. This diagnostic technique can be used for automatic control of the beam movement and its correction. Larger amount of gas are needed for optical diagnostics of a beam of positive ions in a high-energy path with a proton energy of ~ 2 MeV. However, in such a case, an increase in the gas pressure in the beam path does not lead to significant losses of the proton beam.

4.4 Results of modeling beam acceleration and transport

The results of numerical simulations of beam motion in the tandem accelerator prototype carried out at the initial stage of the research are presented in [126]. The simulation was performed using the ExtraSAM program [127], which makes it possible to take into account both the transverse and longitudinal fields of the ion beam space charge. With the space charge taken into consideration, the electrostatic focusing lens at the entrance to the accelerator has a focal length comparable to the size of the inter-electrode gap. The coordinated beam input into the accelerator with compensation for the focusing action of the input electrostatic lens is achieved by introducing a strongly divergent ion beam with a small radius into the accelerator. Such a beam is obtained by refocusing it with a magnetic lens just before entering the accelerator. The simulation was carried out at a negative ion beam current up to 40 mA. At this current, a noticeable rise in beam emittance at the input due to the nonlinear action of space charge forces was observed.

Further numerical simulations were conducted in three-dimensional geometry using the COMSOL Multiphysics 5.3 software without taking into account space charge effects, since the currents of injection into the tandem were lower than 10 mA. Beam motion was studied in accelerator variants with an ion source developed by D-Pace Inc. and with a Penning source developed at the BINP SB RAS described above. Calculations were made only for the low energy path and the tandem accelerator. For the purpose of modeling, the voltage at the high-voltage electrode was assumed to be 1 MV. In these versions, an accelerating tube (pre-accelerator) was used to increase the energy of injection into the tandem. The increased injection energy improves the beam transport at the tandem input and at the same time makes it possible to increase the proton beam energy at the tandem output. The beam particle trajectories obtained as a result of simulation are shown in Figs 18. The beam halo is cut off by the
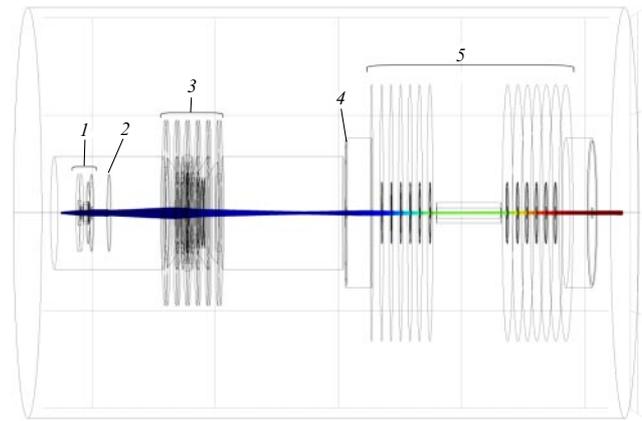
Figure 18. (Color online.) Beam particle trajectories in an accelerator with a D-Pace ion source. *1* — ion source, *2* — output collimator of the source, *3* — pre-accelerator, *4* — input collimator of the accelerator, *5* — accelerator.

collimator at the output of the ion source. Calculations showed that $\sim 20\%$ of the beam current generated by the source of negative ions falls on this collimator.

4.5 Main results of accelerator prototype testing

At the initial stage of the experiments, the emittance of the negative ion beam was measured using a scanner installed in the diagnostic volume close to the ion source. The results of the measurement for the studied version of the ion source are presented in Fig. 19. The measured beam emittance at currents up to 10 mA did not exceed 60 mm mrad, which is less than the acceptance of an accelerator with a system for additional beam acceleration.

When working with the modernized version of the tandem accelerator, algorithms to smoothly change the beam current were evaluated, which required synchronous alteration of ion source parameters and beam duct elements (Fig. 20). A certain reduction in the efficiency of beam transport associated with the increase in current strength was documented. In this case, the current to the input diaphragm of the tandem and the currents to the electrodes of the beam position sensors changed approximately in proportion to the input current toward the accelerator. The reason for the decrease in the beam transport efficiency with increasing current may be the respective rise in beam emittance, leading to enhanced beam losses at the

Figure 19. (Color online.) (a) Beam size, tilt, and angular divergence. (b) Beam emittance in various coordinates.

Figure 21. (Color online.) Neutron generator with a low-energy beam path, the tandem accelerator, a high-energy beam path, and a system for distributing the beam through channels at the neutron-generating target in rooms for patient irradiation.

and the stripping target were substantially redesigned to reduce the strength of the electric field in critical places, improve the adjustment accuracy, and intensify cooling. In addition, an easier-to-operate volumetric source with high beam current was used instead of the surface-plasma source of negative ions. For better agreement with the optics of the tandem accelerator, the beam energy at its entrance was significantly increased. Compared with the prototype, the capabilities of diagnostic and control systems were noticeably expanded. To enable therapeutic sessions in two rooms, the design of the high-energy beam duct has been changed accordingly.

The commercial version of the neutron generator provides a proton beam energy up to 2.5 MeV with a direct current of 10 mA. A general view of the setup with beam splitting into two procedural rooms is presented in Fig. 21. The neutron generator includes a low-energy duct, the tandem accelerator itself, and a high-energy beam duct, allowing the beam to be redirected to several treatment rooms.

The source of negative hydrogen ions is located on a high-voltage platform connected to the accelerating tube, which makes it possible to increase the energy of the beam injected into the tandem to 120–180 keV. Such pre-acceleration of the negative ion beam allows its 'softer' injection into the accelerator which, in turn, permits reducing the effect of strong transverse electric fields at the input to the accelerator on the beam dimensions during its motion in the electrode system. Moreover, the influence of the space charge on beam transport is decreased. In the accelerator prototype described in Section 4, the injection of a low-energy beam into the accelerator resulted in strong focusing. To compensate for this effect, strong refocusing of the beam before the entrance is performed with the help of a solenoid lens. Moreover, the increase in beam energy at the entrance to the accelerator makes it possible to reduce the accelerating voltage at the high-voltage electrode of the accelerator, which also significantly improves the reliability of its operation.

The high-energy beam duct includes magnetic lenses and a splitter for directing the 2.5-MeV proton beam from the tandem accelerator toward lithium targets located in the procedural rooms. The design of the cooling system of the lithium target makes possible the removal of heat from the target under a load of several megawatts per m^2 without melting the lithium layer.

A set of turbomolecular pumps is used to maintain the required vacuum in the accelerator during the operation of the ion source and the stripping target. The pressure in the high-energy duct is maintained at a level of $\sim 10^{-6}$ Torr

Figure 20. Accelerator parameters at fast beam recovery: (a) beam current at the accelerator output; (b) efficiency of beam routing through the tandem — ratio of beam currents at tandem output and input; (c) total accelerating voltage (proton beam energy).

accelerator electrodes. Apparently, the heating of the gas in the stripping target also makes its contribution, resulting in a decrease in density and, hence, a degree of beam stripping.

5. Commercial source of neutrons for clinical trials of boron neutron capture therapy

Based on the data obtained in experiments with the BINP neutron source prototype, TAE Life Sciences (Foothill Ranch, California, USA) has developed, with the support of BINP, a commercial version of the neutron generator for conducting BNCT under clinical conditions. The starting point for the development of the commercial neutron generator was the concept illustrated by Fig. 12. This generator uses a more compact high-voltage source than does the prototype, the sections of which are connected directly to tandem electrodes. Both the tandem electrodes

(without gas puffing in the system for optical diagnostics of beam position and dimensions).

The commercial version of the neutron generator is equipped with an automation system that ensures ease of use of the device in a clinical setting. A multi-stage protection system ensures the safety of the patient and medical personnel in the event of a malfunction of the equipment. The commercial neutron generator is built in compliance with international norms and standards adopted for radiation therapy instruments.

TAE Life Sciences plans to install the first BNCT complex in a new center at Xiamen Humanity Hospital (Xiamen, China). The neutron generator will be a key element of the therapeutic facility, owned and operated by Neuboron Medtech Ltd. (Nanjing, China) in the framework of the BNCT center.

6. Conclusion

Experiments with an accelerator-based neutron generator for BNCT have been carried out at the Budker Institute of Nuclear Physics BSB RAS since 2006. Neutrons are generated as an accelerated proton beam with an energy of ~ 2 MeV and a current up to 9.6 mA drops onto a lithium target. The proton beam is obtained using a tandem accelerator of an original design without accelerating tubes. Biomedical experiments include irradiation of cellular structures and laboratory animals. The neutron generator prototype was used by TAE Life Sciences jointly with BINP to create its compact commercial version with a proton beam energy up to 2.5 MeV and current up to 10 mA. It will be used in the near future to conduct clinical trials of BNCT.

References

1. Barth R F et al. *Clinic. Cancer Res.* **11** 3987 (2005)
2. Moss R L *Appl. Radiat. Isot.* **88** 2 (2014)
3. Sauerwein W A G et al. (Eds) *Neutron Capture Therapy. Principles and Applications* (Heidelberg: Springer, 2012)
4. Farr L E et al. *Am. J. Roeng. Ther. Nucl. Med.* **71** 279 (1954)
5. Goldwin J T *Cancer* **8** 601 (1955)
6. Slatkin D N *Brain* **114** 1609 (1991)
7. Hawthorne M F, Shelly K, Wiersema R J (Eds) *Frontiers in Neutron Capture Therapy* Vol. 1 (New York: Springer-Verlag, 2001) https://doi.org/10.1007/978-1-4615-1285-1
8. Soloway A H, Hatanaka H, Davis M A *J. Med. Chem.* **10** 714 (1967)
9. Hatanaka H *Basic Life Sci.* **54** 15 (1990)
10. Mishima Y et al. *Basic Life Sci.* **50** 251 (1989)
11. Granada A D et al. *Neurosurgery* **44** 1182 (1999)
12. Busse P M et al. *J. Neurooncol.* **62** 111 (2003)
13. Sauerwein W, Zurlo A *Eur. J. Cancer* **38** (Suppl. 4) 31 (2002)
14. Joensuu H et al. *J. Neurooncol.* **62** 123 (2003)
15. Capala J et al. *J. Neurooncol.* **62** 135 (2003)
16. Dbaly V et al. *Ces. Slov. Neurol. Neurochir.* **66–69** 60 (2002)
17. Nakagawa Y et al. *J. Neurooncol.* **62** 87 (2003)
18. González S J et al. *Appl. Radiat. Isot.* **61** 1101 (2004)
19. Kato I et al. *Appl. Radiat. Isot.* **61** 1069 (2004)
20. Kankaanranta L et al. *Int. J. Radiat. Oncol. Biol. Phys.* **82** (1) E67 (2012)
21. Tamura Y et al. *J. Neurosurg.* **105** 898 (2006)
22. Suzuki M et al. *Radiotherapy Oncol.* **88** (2) 192 (2008)
23. Suzuki M et al. *Jpn. J. Clin. Oncol.* **37** 376 (2007)
24. Blue T, Yanch J *J. Neurooncol.* **62** 19 (2003)
25. Kreiner A J et al. *Rep. Pract. Oncol. Radiotherapy* **21** 2 (2016)
26. Tanaka H et al. *Appl. Radiat. Isot.* **67** S258 (2009)
27. Tanaka H et al., in *Proc. of the 14th Intern. Congress on Neutron Capture Therapy, 14ICNCT, Buenos Aires, Argentina, 25–29 October 2010*, p. 447
28. Beynon T, in *Research and Development in Neutron Capture Therapy* (Eds M W Sauerwein, R Moss, A Wittig) (Bologna: Monduzzi Editore, Intern. Proc. Division, 2002) p. 225
29. Wangler T "Conceptual design of an RFQ accelerator-based neutron source for boron neutron capture therapy", LAUR89-912 (Los Alamos: Los Alamos National Laboratory, 1989); *Particle Accelerator Conf., Chicago, IL, March 20–23, 1989*, p. 678
30. McMichael G E, Yule T J, Zhou X-L *Nucl. Instrum. Meth. Phys. Res. B* **99** 847 (1995)
31. Kreiner A J et al., in *Proc. of the 8th Intern. Topical Meeting on Nuclear Applications and Utilization of Accelerators, Pocatello, Idaho, 2007*, p. 373
32. Kreiner A J et al. *Appl. Radiat. Isot.* **67** S266 (2009)
33. Smick T et al., in *Book of Abstracts of the 16th Intern. Congress on Neutron Capture Therapy, Finland, Helsinki, 2014*, p. 138
34. Tsuchida K et al., in *Book of Abstracts of the 16th Intern. Congress on Neutron Capture Therapy, Finland, Helsinki, 2014*, p. 206
35. Forton E et al. *Appl. Radiat. Isot.* **67** S262 (2009)
36. Bayanov B F et al. *Nucl. Instrum. Method. Phys. Res. A* **413** 397 (1998)
37. Dimov G I et al. *Atom. Energy* **94** 116 (2003); *Atom. Energ.* **94** 155 (2003)
38. Miyatake S et al. *J. Neurooncol.* **149** 1 (2020)
39. Hirose K et al. *Int. J. Rad. Onc. Biol. Phys.* **105** E374 (2019)
40. Barth R F, Mi P, Yang W *Cancer Commun.* **38** 35 (2018)
41. Crossley E L et al. *Mini Rev. Medic. Chem.* **7** 303 (2007)
42. Lesnikowski Z J et al. *Bioorg. Medic. Chem.* **13** 4168 (2005)
43. Ahrens V M et al. *Chem. Med. Chem.* **10** 164 (2015)
44. Yang W et al. *Clinic. Cancer Res.* **14** 883 (2008)
45. Kueffer P J et al. *Proc. Natl. Acad. Sci. USA* **110** 6512 (2013)
46. Yinghuai Z et al. *Curr. Chem. Biol.* **1** 141 (2007)
47. Mi P et al. *J. Control. Release* **254** 1 (2017)
48. Sivaev I B et al. *Eur. J. Inorg. Chem.* **11** 1433 (2009)
49. Davydenko V I et al. *AIP Conf. Proc.* **763** 332 (2005)
50. Aleinik V I et al. *Prib. Tekh. Eksp.* (5) 5 (2013)
51. Belchenko Yu I, Grigoryev E V *Rev. Sci. Instrum.* **73** 939 (2002)
52. Belchenko Yu I, Savkin V Y *Rev. Sci. Instrum.* **75** 1704 (2004)
53. Belchenko Yu I et al. *Rev. Sci. Instrum.* **79** 02A521 (2008)

54. Belchenko Yu I et al. *Phys. Usp.* **61** 531 (2018); *Usp. Fiz. Nauk* **188** 595 (2018)
55. Belchenko Yu I et al. *AIP Conf. Proc.* **2011** 050021 (2018)
56. Sanin A L et al. *AIP Conf. Proc.* **2052** 050012 (2018)
57. Bykov T et al. *AIP Conf. Proc.* **2052** 050013 (2018)
58. Belchenko Yu I et al. *Rev. Sci. Instrum.* **77** 03A527 (2006)
59. Belchenko Yu I, Sanin A L, Ivanov A A *AIP Conf. Proc.* **1097** 214 (2009)
60. Belchenko Yu I et al. *AIP Conf. Proc.* **1515** 448 (2013)
61. Belchenko Yu I et al. *Rev. Sci. Instrum.* **85** 02B108 (2014)
62. Barnet C et al. "Atomic Data for Controlled Fusion Research", ORNL-5206 (Oak Ridge, TN: Oak Ridge National Laboratory, 1977)
63. Aleinik V I et al. *Nauch. Vestn. Novosibirsk. Gos. Tekh. Univ.* **50** (1) 83 (2013)
64. Jacob S A W, Suter M, Synal H-A *Nucl. Instrum. Meth. Phys. Res. B* **172** 235 (2000)
65. Egorova V A et al. "Matematicheskaya model' vzaimodeistviya protonov s veshchestvom" ("A mathematical model of proton interaction with matter"), Preprints No. 138 (Moscow: Keldysh Institute of Applied Mathematics, 2017) http://doi.org/10.20948/prepr-2017-138
66. Bayanov B F, Belov V P, Taskaev S Yu "Neitronogeneriruyu-shchaya mishen' uskoritel'nogo istochnika neitronov dlya neitro-nozakhvatyvayushchei terapii" ("The neutron-generating target of the accelerator-based neutron source for neutron capture therapy"), Preprint No. 2005-4 (Novosibirsk: Budker Institute of Nuclear Physics of Siberian Branch Russian Academy of Sciences, 2005)
67. Bayanov B *Appl. Radiat. Isot.* **61** 817 (2004)
68. Bayanov B F, Zhurov E V, Taskaev S Yu *Instrum. Exp. Tech.* **51** 147 (2008); *Prib. Tekh. Eksp.* (1) 160 (2008)
69. Kasatov D *JINST* **15** P10006 (2020)
70. Bayanov B F et al. *Instrum. Exp. Tech.* **51** 438 (2008); *Prib. Tekh. Eksp.* (3) 119 (2008)
71. Kasatov D et al. *Appl. Radiat. Isot.* **106** 38 (2015)
72. Bykov T et al. *Appl. Radiat. Isot.* **175** 109821 (2021)
73. Kasatov D A "Issledovanie materialov neitronogeneriruyushchei misheni dlya bor-neitronozakhvatnoi terapii" ("The study of materials of neutron-generating target for boron-neutron capture therapy"), PhD Thesis (Phys.-Math. Sci.) (Novosibirsk: Budker Institute of Nuclear Physics of Siberian Branch Russian Academy of Sciences, 2022)
74. Batrutdinov A et al. *Metals* **7** (12) 558 (2017)
75. Akhmetov T D et al. *Rev. Sci. Instrum.* **77** 03C106 (2006)
76. Barker P H et al. *Metrologia* **39** 371 (2002)
77. Biesiot W, Smith Ph B *Phys. Rev. C* **24** 2443 (1981)
78. Vartsky D et al. *Nucl. Phys. A* **505** 328 (1989)
79. Burdakov A V et al. *Instrum. Exp. Tech.* **60** 522 (2017); *Prib. Tekh. Eksp.* (4) 70 (2017)
80. Kuznetsov A S et al. *Tech. Phys. Lett.* **35** 346 (2009); *Pis'ma Zh. Tekh. Fiz.* **35** (8) (2009)
81. Aleinik V I et al. *Instrum. Exp. Tech.* **56** 497 (2013); *Prib. Tekh. Eksp.* (5) 5 (2013)
82. Bykov T et al., in *6th Intern. Symp. on Negative Ions, Beams and Sources, NIBS'18, September 3–7, 2018, Novosibirsk, Russia*
83. Taskaev S Yu et al., in *Proc. of the 9th. Particle Accelerator Conf., Vancouver, Canada, MOPML062, 2018*, https://doi.org/10.18429/JACoW-IPAC2018-MOPML062
84. Aleynik V et al. *Appl. Radiat. Isot.* **69** 1639 (2011)
85. Sorokin I N "Vysokovol'tnaya prochnost' uskoritelya-tandema s vakuumnoi izolyatsiei" ("High-voltage strength of accelerator-tandem with vacuum insulation"), PhD Thesis (Tech. Sci.) (Novosibirsk: Budker Institute of Nuclear Physics of Siberian Branch Russian Academy of Sciences, 2014)
86. Sorokin I N, Taskaev S Yu *Instrum. Exp. Tech.* **57** 377 (2014); *Prib. Tekh. Eksp.* (4) 5 (2014)
87. Bykov T A et al. *Instrum. Exp. Techn.* **61** 713 (2018); *Prib. Tekh. Eksp.* (5) 90 (2018)
88. Ivanov A A et al. *Tech. Phys. Lett.* **42** 608 (2016); *Pis'ma Zh. Tekh. Fiz.* **42** (12) 1 (2016)
89. Kasatov D A et al. *Phys. Part. Nuclei Lett.* **13** 954 (2016); *Pis'ma Fiz. Elem. Chast. At. Yad.* **13** 7 (2016)
90. Hasselkamp D et al. *Nucl. Instrum. Meth.* **180** 349 (1981)
91. Sternglass E J *Phys. Rev.* **108** 1 (1957)
92. Brusilovskii B A *Kineticheskaya Ionno-Elektronnaya Emissiya* (Kinetic Ion-Electron Emission) (Moscow: Energoatomizdat, 1990)
93. Ivanov A A et al. *JINST* **11** P04018 (2016)
94. Kuznetsov A S et al. "Pervye eksperimenty po registratsii neitronov na uskoritel'nom istochnike dlya bor-neitronozachvatnoi terapii" ("The first experiments on the registration of neutrons on an accelerator source for boron-neutron capture therapy"), Preprint BINP 2008-27 (Novosibirsk: Budker Institute of Nuclear Physics of Siberian Branch Russian Academy of Sciences, 2008)
95. Kasatov D et al. *J. Instrum.* **9** P12016 (2014)
96. Taskaev S Yu et al., in *Proc. of the 9th Intern. Particle Accelerator Conf., Canada, Vancouver, 2018*, MOPML063, https://doi.org/10.18429/JACoW-IPAC2018-MOPML063
97. Batrutdinov A et al. *Metals* **7** (12) 558 (2017)
98. Zaidi L et al. *Phys. Atom. Nucl.* **80** 60 (2017); *Yad. Fiz.* **80** 63 (2017)
99. Zaidi L et al. *Appl. Radiat. Isot.* **139** 316 (2018)
100. Bayanov B F et al. *Instrum. Exp. Tech.* **53** 883 (2010); *Prib. Tekh. Eksp.* (6) 117 (2010)
101. Aleinik V I et al. *Instrum. Exp. Tech.* **57** 381 (2014); *Prib. Tekh. Eksp.* (4) 9 (2014)
102. Porosev V, Savinov G *JINST* **14** P06003 (2019)
103. Bykov T et al. *JINST* **14** P12002 (2019)
104. Gubanova N et al., in *Book of Abstracts of the 16th Intern. Congress on Neutron Capture Therapy, Finland, Helsinki, 2014*, p. 205
105. Taskaev S Yu, Kanygin V V *Bor-Neitronozakhvatnaya Terapiya* (Novosibirsk: Izd. SO RAN, 2016)
106. Kanygin V V et al. *J. Siberian Med. Sci.* (5c) 5 (2016)
107. Yarullina A I et al. *Tichookeanskii Med. Zh.* (4) 6 (2015)
108. Shoshin A et al. *IEEE Trans. Plasma Sci.* **48** 1474 (2020)
109. Massironi A (CMS Collab.) "Precision electromagnetic calorimetry at the energy frontier: CMS ECAL at LHC Run 2", arXiv:1510.02745
110. Zhang Z *JINST* **13** C04013 (2018)
111. Kasatov D A et al. *Instrum. Exp. Tech.* **63** 611 (2020); *Prib. Tekh. Eksp.* (5) 5 (2020)
112. Kuznetsov A S et al. *Nucl. Instrum. Meth. Phys. Res. A* **606** 3 (2009)
113. Rostoker N, Qerushi A, Binderbauer M *J. Fusion Energy* **22** 83 (2003)
114. Farrell J et al., in *7th Intern. Workshop on Positron and Positronium Chemistry, Knoxville, USA, 2002*, p. 47
115. Sorokin I N, Taskaev S Yu *Appl. Radiat. Isot.* **106** 101 (2015)
116. Taskaev S Yu, Kanygin V V "Sistema formirovaniya puchka neitronov" ("The system for the formation of a beam of epithermal neutrons"), Patent RF No. 2540124, 16.12.2014 (2014)
117. Aleynik V et al. *Appl. Radiat. Isot.* **88** 177 (2014)
118. Taskaev S Yu "Sposob polucheniya puchka epiteplovykh neitro-nov" ("The method for obtaining a beam of epithermal neutrons"), Patent RF No. 2722965, 05.06.2020 (2020)
119. Lee C L, Zhou X-L *Nucl. Instrum. Meth. Phys. Res. B* **152** 1 (1999)
120. Domarov E V et al. *Instrum. Exp. Tech.* **60** 70 (2017); *Prib. Tekh. Eksp.* (1) 77 (2017)
121. Popov S S et al. *Rev. Sci. Instrum.* **91** 013311 (2020)
122. Fraser J S *IEEE Trans. Nucl. Sci.* **28** 2137 (1981)
123. Chamberlin D D, Hollabaugh J S, Stump C J *IEEE Trans. Nucl. Sci.* **30** 2201 (1983)
124. Pasqualotto R et al. *Fusion Eng. Des.* **88** 1253 (2013)
125. Delogu R S et al. in *IEEE Trans. Plasma Sci.* **42** 1802 (2014)
126. Derevyankin G E et al. "Ionno-opticheskii trakt 2.5 MeV 10 mA uskoritel'nogo tandema" ("The 2.5 MeV 10 mA ion-optical tract of the accelerating tandem"), Preprint BINP 2002-24 (Novosibirsk: Budker Institute of Nuclear Physics of Siberian Branch Russian Academy of Sciences, 2002)
127. Tiunov M A, Kuznetsov G I, Batazova M A *AIP Conf. Proc.* **572** 155 (2001)